Future dust concentration over the Middle East and North Africa region under global warming and stratospheric aerosol intervention scenarios

Seyed Vahid Mousavi[1], Khalil Karami[2], Simone Tilmes[3], Helene Muri[4], Lili Xia[5], Abolfazl Rezaei[1,6]

[1]Center for Research in Climate Change and Global Warming, Institute for Advanced Studies in Basic Sciences, Zanjan, Iran.
[2]Leipzig Institute for Meteorology, University of Leipzig, Germany
[3]National Center for Atmospheric Research, Boulder, CO, USA.
[4]Industrial Ecology Programme, Department of Energy and Process Engineering, Norwegian University of Science and Technology, Trondheim, Norway.
[5]Department of Environmental Sciences, Rutgers University, New Brunswick, USA.
[6]Departmant of Earth Sciences, Institute for Advanced Studies in Basic Sciences, Zanjan, Iran.

Correspondence to: Seyed Vahid Mousavi (v.mousavi33@email.com)

Abstract. The Middle East and North Africa (MENA) is the dustiest region, in the world and understanding the projected changes in the dust concentrations in the region is crucially important. Stratospheric aerosol injection (SAI) geoengineering aims to reduce global warming, by increasing the reflection of a small amount of the incoming solar radiation to space, and hence reducing the global surface temperatures. Using the output from the Geoengineering Large Ensemble Project (GLENS) project, we show a reduction in the dust concentration in the MENA region under both global warming (RCP8.5) and GLENS-SAI scenarios compared to the present-day climate. This reduction in dust over the whole MENA region is stronger under the SAI scenario, except over dust hotspots and for the dry season (e.g., summer with the strongest dust events), which more reduction has been projected for the global warming scenario compared with the SAI scenario. The maximum reduction of the dust concentrations in the MENA region (under both the global warming and SAI) is due to the weakening of the dust hotspots emissions from the sources of the Middle East. Further analysis of the differences in the surface temperature, soil water, precipitation, leaf area index, and near surface wind speed provides some insights into the underlying physical mechanisms that determine the changes in the future dust concentrations in the MENA region. Detailed correlation analysis over dust hotspots indicates that lower future dust concentrations are affected by lower wind speed and higher precipitation in these regions, under both RCP8.5 and SAI scenarios.

1 Introduction

Dust aerosols have a great potential to influence the Earth's climate system (Alpert et al., 1998; Middleton et al., 2017; Wang et al., 2017; Kok et al., 2018), including directly scattering of short-wave radiation, absorption of long-wave radiation (Dufresne et al., 2002; Albani et al., 2014; Mahowald et al., 2014; Kok et al., 2017), and indirectly changing

cloud properties and precipitation rates through aerosol-cloud interaction (Atkinson et al., 2013; Sagoo et al., 2017). Furthermore, dust deposition in different environments (particularly on ice and snow) may affect the surface albedo (Krinner et al., 2006; Painter et al., 2013; Albani et al., 2018; Sarangi et al., 2020). Mineral dust may also be transported

35 a long distance and affects areas apart from the emission source, such as the biogeochemistry of the oceans, and hence induces feedbacks within the climate system (Jickells et al., 2005; Cao et al., 2005; Gasso et al., 2010; Wang et al., 2017; Kok et al., 2018). The dust storms can further influence the human health, agriculture, and transport sectors, particularly in the arid and semi-arid regions (Alboghdady et al., 2016; Sternberg et al., 2017). In the Northern Hemisphere (NH), the Middle East and North Africa (MENA) regions, including Sahara and the Middle East, are important sources for the dust

40 emission. The MENA region is part of the NH "dust belt", which extends from North Africa to East Asia which is evident from satellite observations (Ginoux et al., 2012). Generally, the MENA region is dry with a weak and scattered vegetation coverage, partially because it is away from the storm-track regions and cannot receive humidity transferred from remote (Karami et al., 2019). The MENA region also accounts for the dustiest region in the world (i.e., northern Chad) and the largest warm desert (Sahara) (Giles et al., 2005). Therefore, it is essential to understand dust concentration changes in this

45 region under different future climate scenarios.

Previous research using different methods and approaches indicates great uncertainty in determining the future changes of the global dustiness. As an example, Tegen et al. (2004) using HADCM3 and ECHAM4 models with IS92a IPCC scenario demonstrated that future dust emissions may increase or decrease. Woodward et al. (2005) using the HadAM3 AGCM model with the IS92a scenario, indicated an increase in the future global dust emissions, while Mahowald et al.

50 (2003) suggested a 20–60% reduction in future dust emissions under six scenarios using the Climate System Model (CSM) 1.0 model from the National Center of Atmospheric Research. Under Representative Concentration Pathway (RCP8.5) scenario and using regional climate model (RegCM4.0) (Giorgi et al. 2012), regional projections over West Africa projected an increase in mineral dust with significant increase over Sahel and Sahara in the warm season (Ji et al., 2015). Liu et al., (2019) projected a reduction in the dust events over Northern China under RCP8.5 scenario using the fifth

55 Climate Models Intercomparison Project (CMIP5). The incorporated dust emission, transport, and both dry and wet depositions (collectively called the dust cycle) are incorporated into climate models and Earth system models which greatly differ in dust emission schemes, vegetation cover for dust emission (either prescribed or prognostic) and assumptions about dust sizes (Wu et al., 2020). While most models have the skill to generate the general patterns of global dust distribution (Liu et al, 2012; Huneeus et al, 2011), however large uncertainties still exist in the simulated global dust

60 budgets estimated by the model results (Huneeus et al., 2011; Textor et al., 2006) which impede the interpretation of the evolution of dust storms under future climate projections (Boucher et al, 2013; Yue et al., 2010). For example, the recent study of Wu et al (2020) analysed 15 models participated in the CMIP5 project and compared them with an aerosol reanalysis as well as station observations and concluded that while the models generally agree with each other as well as observations in producing the NH dust belt, the models greatly differ in the spatial extent of the dust belt and have large

65 biases in dust deposition regions for some models.

Slow progresses in decoupling anthropogenic emissions from economic growth and negative emission technologies are the main reasons for continuation of the increase in the global atmospheric greenhouse gas concentration (Fuss et al., 2014; Rozenberg et al., 2015; Sanderson et al., 2016). Moreover, previous research indicates that the current pledges to reduce greenhouse gas emissions would not be sufficient to limit temperature rise beyond 1.5-2°C (compared to the pre-industrial period) (Millar et al., 2017; Pasztor and Turner., 2018). Geoengineering is considered as the third pillar of climate change policy (alongside mitigation and adaptation efforts) to compensate for anthropogenic warming (e.g., Nurse, 2011; Macnaghten and Szerszynski., 2013), and Stratospheric Aerosol Injection (SAI) geoengineering is one of the most discussed strategies. In other words, SAI is an interim measure to offset warmings while the emissions are reduced. Among various geoengineering approaches, SAI has received a particular attention for mainly two reasons a) volcano eruptions may serve as a natural analogy for this strategy, and b) all modelling studies show an efficient global cooling effect with the SAI strategy (e.g., Caldeira and Matthews, 2007; Robock et al., 2008; McClellan et al., 2010; Tilmes et al., 2018; Simpson et al., 2019; Visioni et al., 2020). Climate models may simulate SAI by injecting sulfate aerosols or their precursor (sulfur dioxide, SO_2) into the stratosphere, which reflects some of the incoming sunlight back to space (Crutzen, 2006; Rasch, 2008). Other types of aerosols are also being investigated, e.g., the sensitivity of the chemistry-climate models to injection of H_2SO_4 instead of SO_2 have been investigated (Keith et al., 2019; Vattioni et al., 2020).

There are many unknowns regarding the SAI and its modelling, particularly its potential side effects on regional and local scales. While some of the debates is focused on the technical, financial, and even political feasibility of such climate intervention scenarios, the lack of knowledge on the potential impacts, including dust concentration change, of such interventions in local scale is still a main cause for concern (Karami et al., 2020). Therefore, there is an immediate need for knowledge on the dust concentrations response to the possible future climate change scenarios in the MENA region. This might assist to inform the local governments and public of the potential impacts of such climate intervention scenarios. Here, we use the data generated by the Geoengineering Large Ensemble Project (GLENS) project (Tilmes et al., 2018) to (1) examine the future changes of dust concentration in the MENA region under RCP8.5 and SAI, and (2) demonstrate the dust relationship with hydro-climate variables of temperature, soil water, precipitation, leaf area index, and near surface wind. The paper is structured as follows: the method and data are presented in Section 2, the results in Section 3, the discussion in Section 4, and the conclusions are finally drawn in Section 5.

2 Data and Methods

In this study, we use the GLENS project output. The GLENS project investigates the impacts of SAI within the climate variability on the global and regional scale with large ensemble members to reach multiple temperature targets using a feedback algorithm (Tilmes et al., 2018). GLENS includes a 20-member ensembles of the baseline RCP8.5 scenario for the period 2010-2030, which serves as a control dataset (hereafter the present-day climate or CTL simulation). Three of the control simulations were continued until 2097, which serves as the baseline simulation. For each ensemble member,

the atmospheric state is initialized with 1 January conditions taken from different years between 2008 and 2012 of the reference simulation and a round-off (order of 10^{-14} K) air temperature perturbation, while the land, sea ice, and ocean start from the same initial conditions for each ensemble member. In addition, there are 20 ensemble members of the SAI simulations from 2020 to 2097. Annually varying SO_2 injections were performed at four locations (30°N, 30°S, 15°N, and 15°S) into the stratosphere (roughly about 5 km above the tropopause) (Kravitz et al., 2017). Sulfur injection amounts for the GLENS simulations are shown in Tilmes et al., 2018 (BAMS paper) in Figure 2. The feedback control algorithm calculates the needed amount of sulfur injections per year for each of the 4 injection locations, as illustrated in Tilmes et al, 2018, Figure 2. To counter the warming of RCP8.5, over 50 Tg SO_2 injections will be needed in total by the end of the 21st century. The amount of injection annually adjusts using a feedback-control algorithm to keep a) the global surface temperature, b) interhemispheric and c) equator-to-pole temperature gradients close to the year 2020 conditions. The interhemispheric surface temperature gradient is defined in equation (1) of Kravitz et al (2017). It is simply the difference between the mean surface temperature in the Northern and Southern hemispheres. In the study of Tilmes et al (2018), the values for the interhemispheric differences for the different periods and scenarios are presented in Table 3 (T1). In the GLENS project, an updated version of the Community Earth System Model CESM Version 1 (Hurrell et al., 2013) with the Whole Atmosphere Community Model (WACCM) as its atmospheric component (Mills et al., 2017) is used. The baseline scenario is the Representative Concentration Pathway 8.5 (RCP8.5) (2010-2097). The SAI scenario (2020-2097) is based on the same baseline emission pathway and uses sulfur dioxide injections to keep surface temperatures at 2020 conditions. The model simulations are performed with horizontal resolution of 0.9° latitude by 1.25° longitude, and 70 vertical layers up to 140 km (~10^{-6} hPa). The three-mode version of the Modal Aerosol Module (MAM3) is used to simulate microphysical processes of the aerosols in the troposphere and stratosphere (Liu et al. 2012) and include prognostic stratospheric aerosols (Mills et al., 2016). WACCM is fully coupled with the Community Land Model, version 4.5 (CLM4.5) (Oelson et al. 2013) as well as with other CESM1 components, are listed in the Table 1. Details of simulations, coupled models, and parametrization are further described by previous researchers (e.g., Danabasoglu et al., 2012; Holland et al., 2012; Guenther et al., 2012; Marsh et al., 2013; Milles et al., 2016; Milles et al., 2017; Tilmes et al., 2018). In the CLM model, Dust Entrainment and Deposition model (DEAD) (Zender et al., 2003) is used for atmospheric dust mobilization scheme (Mahowald et al. 2006; Oleson et al., 2013). Based on the DEAD, the total vertical mass flux of dust (Fj) from the ground into transport bin j is computed by

$$F_j = TSf_m \alpha Q_s \sum_{i=1}^{I} M_{i.j} \tag{1}$$

where T is a global factor, S the source erodibility factor, f_m grid cell fraction of exposed bare soil suitable for dust mobilization, α sandblasting mass efficiency, Q_s the total horizontally saltating mass flux of "large" particles, and $M_{i,j}$ the mass fraction of each source mode i carried in each of $J = 4$ transport bins j.

The value of f_m factor and ability of dust to mobilize are highly decreased by increasing the total water content (including

130   lake, wetlands, and soil moisture) as well as the fraction of vegetation cover in each grid cell (Oelsen et al., 2013), based

on $f_m = (1 - f_{lake} - f_{wetl})(1 - f_{sno})(1 - f_v)w_{liq,1}/(w_{liq,1} + w_{ice,1})$ where $f_{lake}, f_{wetl}, f_{sno}$ and f_v are the grid cell

fractions of lake, wetland, snow cover, and vegetation cover, respectively. $w_{liq,1}$ and $w_{ice,1}$ represent the top soil layer

liquid water and ice contents, respectively. In practice, soil moisture controls the threshold wind friction speed for saltation.

Further, the total horizontally saltating mass flux (Q_s) is related to the third power of the wind speed; thus, any changes in

135   wind speed could affect the dust emissions (Tegen and Fung, 1994; Tegen et al., 2002; Zender et al., 2003; Oelsen et al.,

2013) with a positive correlation. Previous studies also show that a higher vegetation coverage leads to smaller dust

emissions as the vegetation coverage can trap soil moisture through its roots and shade and also reduce soil erosion by

reducing wind friction (Hillel et al., 1982; Raupach et al., 1994; Nicholson et al., 1998; Zender et al., 2003). In other

words, the total Leaf area index (TLAI) have a negative correlation with dust emissions and subsequently with atmospheric

140   dust which is also depicted in the result section. The dust model also consists of removing mineral dust from the

atmosphere, including dry deposition and wet deposition. Wet deposition removes dust aerosols through in-cloud and

below-cloud precipitation process (Albani et al., 2014; Zender et al., 2003). In practice, precipitation has a negative

correlation with atmospheric dust concentration, as discussed below. Although the temperature does not directly contribute

to the dust flux equation in the CLM model, increasing the temperature leads to lower soil moisture (Seneviratne et al.,

145   2010) and a higher possibility for dust emission. For more details about parametrizations and calculations, the readers are

encouraged to see (Zender et al., 2003, and Oelsen et al., 2013).

From the model outputs, we derived all available columnar dust burden dataset (ranging from 0.058 µm to 3.65 µm) by

the summation of the mean monthly values of the accumulation mode (particle size from 0.058 to 0.27 µm) and the coarse

mode (particle size from 0.8 to 3.65 µm). The geographical focus of the current study's latitude and longitude is 15 °N to

150   45 °N and 20 °W to 62.5 °E (hereafter referred to as the MENA region). Figure 1 shows the population density map over

the MENA region (available from the Socioeconomic Data and Applications Center (SEDECA) a data center in the

National Aeronautics and Space Administration (NASA) (https://sedac.ciesin.columbia.edu/)). We further focus on the

Middle East region (20 °N to 45 °N and 45 °E to 62.5 °E) since it has a higher population and is sensitive to changes in

the dust events, as discussed in the introduction. Furthermore, we focus over the regions with higher dust concentrations

155   as dust hotspots. Here, we use the regional and temporal averaged monthly surface temperature, near surface wind speed,

precipitation, soil water, and total leaf area index between 2010 to 2097 to investigate the possible changes in the dust

concentrations. The dust concentration is controlled by above-mentioned variables. Here, we calculated the differences

between CTL, RCP8.5 and SAI simulations to identify the important factors that influence the temporal and spatial

changes of the dust concentration under the above-mentioned scenarios. In this study, all available ensemble members of

160   the GLENS project are used to represent the present-day climate or CTL (2010-2029 period), the global warming climate

or RCP8.5 (2078-2097 period), and the future climate under GLENS-SAI (2078-2097 period) simulations. Table 2

represents the different simulations, acronyms, number of ensemble members, and period of the analyses used in this study. We also carried out the t-test with (99.9% confidence level) to determine whether the differences between RCP8.5, SAI, and CTL simulations are significant. In all contour plots, regions with a confidence level of more than 99.9% are indicated with hatch lines (i.e., differences in these regions are significant). In this study, the independent t-test analysis has been used for comparing the statistical difference between scenarios for considered parameters. T-test analysis is a statistical test that is used to determine the statistically significant difference. Depending on the confidence level, the obtained t-value can be lower or higher than the statistical analysis threshold (t-value). If the t-value is lower than the critical value, there is no statistically significant difference between samples, and if it is higher than the critical value there is a statistically significant difference between them. The t-value depends on the means and variabilities of the two datasets (i.e., means, variances, and the number of samples in different scenarios). In this investigation, the t-test is performed for 20 years (60 months for seasonal and 240 months for annual difference). The t-test formula is given in equation 1, where X_1 and X_2 are the means, S_1^2 and S_2^2 are the variances and n_1 and n_2 are the number of samples,

$$t - value = \frac{|\overline{X_1} - \overline{X_2}|}{\sqrt{\frac{S_1^2}{n_1} + \frac{S_2^2}{n_2}}} \qquad (2)$$

For more detail about statistical analysis reader, the readers are encouraged to see (Miller. J. N. and Miller. J. C., 1998). Furthermore, the spatial average of annual time series over dust hotspots are used to visualize the annual trends by the end of this century.

We also calculate the correlation coefficient of dust with other considered parameters for all grids (i.e., cells with a horizontal resolution of 0.9° latitude by 1.25° longitude) over the MEAN region, for both RCP8.5 and SAI scenarios. The climatology of dust concentration is used to specify dust hotspots regions and regions with columnar dust concentration lower than 35 ($\mu g/m^3$) are depicted with hatch-line in the correlation coefficient figures. Moreover, the spatial average of annual time series over dust hotspots are used to calculate the correlation coefficients of atmospheric dust concentration with surface temperature, near-surface wind speed, total leaf area index, precipitation, and soil water for both RCP8.5 (2010-2097) and SAI (2020-2099) scenarios and are listed in Table 3.

3 Result

3.1 Atmospheric Dust Concentrations change under Different Scenarios

Fig. 2a shows the seasonal cycle of monthly regional mean values. The dust reduction in the MENA region for both the SAI and RCP8.5 scenarios (compared to the CTL simulation) is stronger during the spring and summer seasons (i.e., about 15%). Fig. 2b shows the annual mean trends of dust concentrations across the MENA region for RCP8.5 (2010-2097),

and SAI (2020-2099). This figure displays that dust mass concentrations tend to decrease in MENA under both the global warming and SAI scenarios by the end of this century, and under SAI scenario, dust mass concentration reduction is about 5% stronger than that in RCP8.5. The climatology of columnar dust mass concentration over the MENA region is derived from all twenty ensembles for the control simulation from 2010 to 2029 (Fig. 2c), which suggests that there are five sub-regions in the MENA region with the highest dust concentrations: Northwest Africa (R1), North Africa (R2), Northeast Africa (R3), Southwest of the Iranian plateau (R4) and Northeast of Iranian plateau (R5). Figures 2d and 2e show the meridional and zonal mean annual dust concentration for the CTL, RCP8.5, and SAI scenarios, which are averaged over the whole MENA region, respectively. Overall, in Fig. 2e, the highest dust concentrations (up to 37 $\mu g/m^3$) are found across North-eastern Africa (i.e., 30-32 °E) and Middle East (i.e., 48-62.5 °E) while in Fig. 2d, the lower latitudes of 15-20 °N (i.e., Northern Africa) have the highest dust (up to 30 $\mu g/m^3$). Notably, these high dust concentrations coincide with the five major dust hotspots of R1 to R5 (Fig. 2c) where among them, R5 is the largest and strongest. Figure 2c shows only a portion of the R5 region while the R5 in combination with R4 constitutes a major dust source for the Middle East. The seasonal mean values of dust concentration under both the SAI and RCP8.5 scenarios are shown for the MENA region (Fig 2f). Figure 2f illustrates that summer and, to a lesser extent, spring have higher dust concentrations than autumn and winter seasons under both the SAI and RCP8.5 scenarios across the whole MENA region.

Fig. 3a-o show seasonal and annual changes of dust mass concentration mean value in the MENA region under different climate scenarios. The differences are represented by the percent of change relative to the maximum number of the annual dust concentration in the MENA region ($DUST_{MAX}$ = 185.75 ($\mu g/m^3$)) in the current climate (CTL). The dashed line contours show dust hotspots (R1 to R5) in the current climate and the regions with hatch line indicates the regions where the changes are more than 99.9% significant level based on the student's t-test analysis. The reduction for the SAI scenario is generally larger than that for the RCP8.5 (Fig. 2b and Fig. 3o), although 5-15 % reduction is found in each dry season under the RCP8.5 scenario compared SAI scenario (Fig. 3g, h and i). The detailed analysis suggests that the maximum reduction of the dust concentrations in the MENA region (in both the global warming and SAI scenarios) mostly results from the weakening of the dust concentration in the Middle East, rather than from the North Africa (Fig. 3d, e, g and h).

3.2 Candidate Variables Change under Different Scenarios

In the following, we determine the contributions from climate changes to dust concentration under different scenarios over the entire MENA region. The annual mean temperature responses to the different scenarios are shown in Fig 4a-c. As expected, in the whole MENA region, surface temperature increases 20-30 % (4.5-6.5 °C) under the high emission scenario (RCP8.5), while under the SAI scenario, there is no statistically significant changes (Fig. 4), (as also shown in Kravitz et al., 2017; Tilmes et al., 2018; MacMartin et al., 2019). Furthermore, the annual mean surface temperature with its standard deviation (indicated by the shaded envelope) for RCP8.5 and SAI scenarios are shown in Fig. 4d from 2010 to 2099. RCP8.5 shows strong temperature increasing, while SAI successfully maintain the average temperature as the level of CTL.

Figure 5 shows the spatiotemporal anomalies of TLAI for the different scenarios of CTL, RCP8.5, and SAI. The TLAI under the RCP8.5 scenario shows 5-30 % reduction compared to the CTL across the different area of MENA region, except the region between the Mediterranean and Caspian Seas (Fig. 5a, d, g and j). The percent of change has calculated relative to maximum number of the TLAI in the current climate ($TLAI_{MAX} = 7.34$). Seasonal cycle plots of TLAI over the whole MENA region (Fig. 5p) show that the TLAI slightly increases during the winter and spring seasons up to 20% (i.e., mostly wet seasons) for RCP8.5 scenario. This increase in the monthly TLAI, despite the decrease in TLAI over the large geographical coverage of the MENA region, reveals that the averaged-TLAI is determined by the values from the Northern MENA region. Over the summer and autumn, there are no statistically significant changes in the mean value of TLAI under the RCP8.5 scenario (Fig. 5p). On the contrary, under the SAI scenario compared to the CTL, the TLAI shows a 20-35 % increase both spatially and temporally (Fig. 5b, e, h, k, p and q). The mean annual TLAI time series with its standard deviation (indicated by the shaded envelope) (Fig. 5q and r) also confirm these results where TLAI has a positive trend under the SAI scenario while it has no change under the RCP8.5. Figure 5r reveals the annual number of the grid cell in the studied region with a TLAI of larger than 0.3 for both SAI and RCP8.5 scenarios. This number is a threshold in the dust module for dust emission. Although Figure. 5r indicates almost 15 % increase in TLAI under SAI simulations, and approximately no change in TLAI under RCP8.5, the shaded envelope depicted the standard deviation of different ensemble members.

The 10-meter wind speed responses to different scenarios are shown in Figure 6. In general, the wind speed tends to decrease under the global warming (RCP8.5) scenario compared to CTL across the whole region (Fig. 6p and q). Despite this reduction across the whole region, during summer there is an increase in the wind speed (up to 20%) under global warming compared to the CTL across 15-30°N, containing the two major dust hotspots of R1 and R3 (Fig. 6g). SAI also shows reductions in the wind speed compared to the CTL during all the seasons, notably in the Middle East with two major dust hotspots, it shows a 5 to 20 % reduction (Fig. 6b, e, h, k, n). Figure 6q further shows that the wind speed with its standard deviation for both the SAI and RCP8.5 scenarios are reduced compared to the CTL, and under SAI this reduction is gradually stronger than RCP8.5 starting from 2050. Fig. 6p show that the decrease in the wind speed under the SAI scenario is larger than that from the global warming scenario over the whole MENA region. Figure 6r shows the annual mean of the near surface wind for all scenarios for different latitude. Furthermore, it is evident that the regions with higher latitudes (>32ºN) are indicated by a reduction in their wind speed under both RCP8.5 and SAI compared to CTL (Fig. 6r).

Figure 7 displays the spatiotemporal differences between the CTL precipitation and those obtained from the RCP8.5 and SAI scenarios. The results suggest that under the RCP8.5 scenario compared to CTL, the precipitation increases across the North Africa up to 25% (relative to maximum precipitation of CTL scenario in the MENA region ($Precipitation_{MAX} = 4.70 \ mm/day$)), in summer and fall seasons (Fig 7g and j). Under SAI simulation compared to the CTL, the Middle East receives a 10 to 25% higher precipitation in winter and spring seasons (Fig. 7b and e). Comparison of the precipitation changes between SAI and RCP8.5 simulations reveals that during the spring season, there

is about 20% enhancement in the precipitation under the SAI simulation compared to the RCP8.5 in parts of the Middle East region (Fig. 7f). The box plot and monthly mean values of the precipitation from different scenarios (Fig. 7p) show that under the RCP8.5 scenario (compared to the CTL), precipitation is projected to almost a 20% increase during the summer season, and under the SAI scenario (compared to the CTL), this region would experience 5 to 25% more precipitation during the spring and summer. The time series of the annual mean precipitation with their standard deviation (indicated by the shaded region) is presented in Fig. 7q. It suggests that the mean annual precipitation across the whole MENA region will increase by 5% under the SAI and RCP8.5 scenarios by the end of this century. Furthermore, Fig. 7r shows that the increased precipitation rate for the RCP8.5 and SAI scenarios are about 25% higher compared to CTL over the Middle East.

The temporal and spatial differences in the top 10 cm soil water for different scenarios are shown in Fig. 8. In general, Fig. 8a, d, g, j, and m depict an increase in the soil water over the North Africa and a decrease across the Middle East under the RCP8.5 scenario (compared to the CTL). On the contrary, under the SAI simulation (compared to RCP8.5), the soil water demonstrates a decrease (i.e., about 30%) over the North Africa and up to 30% increase across the Middle East (particularly during the spring season). Figures 8p and 8q show the box plot with monthly mean values and annual trends with standard deviation of the soil water for different scenarios. In the wet seasons (winter and spring), the soil water for the RCP8.5 is 5% lower than the CTL, while the SAI simulation shows up to 5% higher values of soil water compared to the CTL (Fig. 8p). Furthermore, Fig 8q shows that a moderate positive trend and slightly negative trend of the annual mean value exists in the soil water under the SAI and RCP scenario, respectively, for whole MENA region.

3.3 Correlation of Atmospheric Dust Concentrations with Candidate Variables

Finally, to find the most efficient factors for reducing columnar dust concentration over hotspots, we calculated the correlation coefficient of dust with other considered parameters for all grids (i.e., cells with a horizontal resolution of 0.9° latitude by 1.25° longitude) over the MEAN region (Fig. 9). The positive and negative correlations are depicted as a contour plot for both RCP8.5 (2010-2097) (Fig. 9, left column) and SAI (2020-2099) (Fig. 9, right column). The detrended annual mean time series is used to calculate the correlation coefficient between dust concentration with other considered parameters. Moreover, the statistical analysis performed on the time series, and regions with a confidence level of more than 99.5% are shown with hatch-line in Fig 9. In Fig. 9a and Fig. 9b, the correlation between dust and wind speed is presented, and positive correlations (i.e., +0.7) are shown over the dust hotspots. The correlation of dust concentration precipitation (Fig. 9c and d) and with soil water (Fig. 9e and f) show negative mean values (i.e., up to -0.35) for the R4 region. Furthermore, negative correlations (i.e., 0.1 to -0.3) between dust and TLAI can be seen for some parts of hotspots in both scenarios (Fig. 9g and h). The correlations between dust and surface temperature are depicted in Fig. 9i and j. Moreover, the spatially averaged correlation coefficients between dust and considered parameters for five dust hotspots over the MEAN region and under both RCP8.5 and SAI scenarios are calculated using detrended annual mean time series and listed in Table. 3. In this table, the most important variables for each region are highlighted in orange. According to

this table, for all dust hotspots (i.e., R1 to R5), the wind speed is the main parameter that affects dust concentration change under both RCP8.5 and SAI scenarios. It seems that the increase in precipitation under both RCP8.5 and SAI scenarios is the other important factor that could affect the reduction of dust concentration in the R5 region.

Moreover, to explore the annual trends of parameters over the dust hotspots, and to compare the annual mean values of different variables, we depicted the regional annual mean of considered parameters under both RCP8.5 and SAI scenarios over different hotspots regions (Fig. 10). Figure 10, indicates that the reduction of dust concentration for R4 (i.e., about 15%) and R5 (i.e., about 20%) under both RCP8.5 and SAI scenarios have been modeled (Fig. 10a4 and a5). Although, the dust concentration over the R2 and R3 hotspots has no considerable change by the end of the century for RCP8.5, an approximately 20% and 10% reduction is projected for the SAI scenario over the R2 and R3 hotspots respectively (Fig. 10a2 and 10a3). Corresponding to the reduction (i.e., about 15%) of dust in R4 region (Fig. 10a4) under both RCP8.5 and SAI scenarios, an increase (i.e., about 50%) in precipitation (Fig. 10c4) and a decrease (i.e., about 5% for RCP8.5) in wind speed (Fig. 10b4) are seen. Detailed analysis of annual trends for the R5 region indicates that the reduction of dust concentration in this region (i.e., about 20%) would be affected by the decrease (i.e., about 5%) in wind speed and the considerable increase (i.e., about 50%) in leaf area index under both RCP8.5 and SAI scenarios (Fig. 10a5, b5, and e5).

Figure 11 included error bars for monthly mean values of all considered parameters for R4 and R5 regions, and shows a reduction of dust concentration between the control and the two future scenarios (up to 25%) for R4 and (up to 35%) for R5 regions in spring to fall (Fig. 11a and b). Differences between RCP.85 and SAI are however not statistically significant. The monthly mean values with error bars of all considered parameters for R1, R2 and R3 regions are also shown in Fig S1. It seems that the reduction of dust concentration over the R4 region (Fig. 11a) has affected by the lower wind speed (Fig. 11c), and higher precipitation (Fig. 11d) and leaf area index (Fig. 11j) under both RCP8.5 and SAI scenarios. Furthermore, the reduction of the monthly mean value of dust concentration over the R5 region (Fig. 11b) could be a result of the decrease in wind speed (Fig. 11d) and increase in leaf area index (Fig 11j). The results of Fig. 10 and Fig. 11, are in good agreement with the results and correlation coefficients in Table 3.

4 Discussion

Based on the CTL simulation, the regions that are highlighted with the dashed-lined contour in Fig 2c (i.e., R1, R2, R3, R4 and R5) are introduced as hotspots of the columnar dust concentration over the MENA region, and this is in agreement with the global-scale atmospheric dust sources determined by previous studies (e.g., Prospero et al, 2002; Ginoux et al., 2012; Middleton 2017). The Saharan desert as the largest warm desert in the world encompasses R1, R2 and R3. Notably, R3 is consistent with the Bodélé Depression in Northern Chad, as the region of highest dust concentrations in the world (Giles et al., 2005). Region R4 also covers some part of Iraq and Iran and this region accounts for one of the important sources of dust emissions in the Middle East region (Prospero et al., 2002; WMO and UNEP, 2013; Cao et al., 2015). Finally, the Central Asia, and the Karakum and Kyzylkum deserts are the main sources of dust storm generation (Orlovsky

et al., 2005), which corresponds to region R5 in Fig 2c. In general, it is found that the locations and concentrations in the dust hotspots regions are realistically simulated by the GLENS. The changes in the dust concentration over the Middle East might be considered even more important than those in the Northern Africa due to its higher population; although the future patterns of the population density may also change. Also, dust activities are more important in the area of interest during summertime with drier and warmer conditions (Fig 2 and 3). As our analysis reveals, the reduction of the future dust mass concentration over the MENA region (in both of the RCP8.5 and SAI scenarios) are mostly due to the weakening of the Middle East dust hotspots (Fig. 2 and 3). Moreover, the highest dust concentration of each year over the MENA region occurs during summertime (Fig. 2f). The reduction rate of the dust concentration is about 5-35% for the RCP8.5 scenario (compared to CTL), where it is stronger from March to September, especially for the dust hotspots in the Middle-East region (Fig. 3d, g, and j). Similarly, the dust concentration is also found to decline 5-30% under the SAI scenario compared to CTL over the dust hotspots in the MENA region (Fig. 3b, e, h, and k). Dust concentrations in the summer of the R3, R4, and R5 hotspot regions under the SAI scenario are approximately 5-15% higher than in the RCP8.5 scenario (Fig. 3i).

As depicted in the result section, the increase in the monthly mean TLAI for the RCP8.5 and SAI scenarios (compared to the CTL), is mostly determined by the values of the quantity in the Northern MENA region. This increase is probably because of CO_2 fertilization, the Northern MENA are covered with vegetation, and higher CO_2 in RCP8.5 and SAI boosts plant growth (Ueyama et al., 2020). The Leaf area index (LAI) is a quantity to characterize the plant canopies (e.g., the aboveground portion of trees, crops, etc.). LAI is a dimensionless quantity and is defined with the following equation; $LAI = one - sided\ leaf\ area\ (m^2)\ /\ ground\ area\ (m^2)$. Fig. 5p demonstrates that the TLAI from the SAI scenario has increased up to ~0.2 (i.e., about 30%) compared to the CTL. In the spatial maps, this increase is projected in the Northern MENA (i.e., southern Europe) with higher annual precipitation (i.e., tropical climate), which contains no dust hotspot. In the Community Land Model, 0.3 has been considered as a threshold of Leaf Area Index (LAI) for the dust emission, and for a region with LAI of less than 0.3, dust emission may be emitted (Mahowald et al., 1999; Zander et al., 2003; Mahowald et al., 2010; Kok et al., 2014). Overall, the total leaf area index is found to increase over the whole MENA region (Fig. 5q and p), and also over the R2, R4 and R5 hotspots regions with higher latitude (Fig. 10, 11, and S1) under both the RCP8.5 and SAI scenarios, whereas the increase under SAI is higher compared to the RCP8.5 scenario. Under RCP8.5, extreme heat and potential extreme drought will prohibit the TLAI from increasing (compared to the SAI), but under SAI, lower temperature will benefit some plants, and also reduce the latent heat which will increase soil water. Although, more than 100% increase of TLAI is projected in R4 and R5 region for both RCP8.5 and SAI scenarios (Fig. 10e4, e5, Fig. 11i and j), the TLAI mean values over R4 and R5 are still lower than the threshold of the dust emission in the dust generation model (i.e., $TLAI_{mean} < 0.3$). However, this small increase may help to decrease the dust concentrations, since based on correlation coefficients in Fig. 9, and Table.3, there is a negative correlation between the dust and TLAI in these regions.

Our results show that over the whole MENA region, the wind speed is generally weaker under SAI simulation compared to RCP8.5 throughout the year (Fig 6p, and q). Figure 6r demonstrates that the wind speed at the higher latitudes considered here (>32 °N), such as the R4 and R5 dust hotspots, would decreases to a larger degree (i.e., about 5%) under both the SAI and RCP8.5 scenarios. This could be a possible reason for the larger reduction in the dust concentrations over the Middle
360   East compared to North Africa under the SAI and RCP8.5 scenarios compared to the CTL (Fig 2, 3, 10 and 11). Such wind change under different climate change scenarios is expected to affect the sub seasonal variability and circulation (Zagar et al., 2020).

R4 dust hotspot will encounter an enhancement in the annual precipitation (i.e., about 100% and 65% under both RCP8.5 and SAI simulations respectively), consistent with an increase TLAI index (i.e., more than 100% under both scenarios)
365   (Fig. 10). In the other word, the R4 region, with a semiarid climate would undergo more precipitation under both RCP8.5 and SAI scenarios (compared to the CTL), which is an important factor on how the dust concentration is determined. In detail, for longitudes > 40 °E (i.e., in the vicinity of R4 and R5), the precipitation differences between the RCP8.5 and SAI with CTL scenarios is about 20-50 mm/year (Fig. 7r). This means that mentioned region receives 20-50% more precipitation in the future climate and this is a considerable amount for this semiarid region.

370   Based on the above analysis, dust emission physically reduces with cooler temperatures, weaker winds, and wetter climates through increasing precipitation and soil water and, in turn, denser and broader vegetation coverage. As explained using Eq. (1), the ability of dust to mobilize highly reduces with greater total water content (Oelsen et al., 2013). The results demonstrate that the dust concentrations in the dust hotspots are substantially affected by wind speed and precipitation more than other parameters. Nonetheless, there are some limitations associated with the present work. First, the GLENS
375   project is based on only one model and a specific SAI injection scenario and applied injection strategy. We suggest to also consider other model results in future studies to reduce the possible uncertainties associated with just using a single one. Moreover, neither the current study nor the GLENS project suggests the SAI as an alternative way for the emission reductions and mitigation efforts. We also point out that the results presented in the current study should not be used as an indication for the real-world large-scale deployment of aerosols in the atmosphere.

380   **5 Conclusions**

This study projects the changes in atmospheric dust mass concentrations in the MENA region under the Stratospheric Aerosol Injection (SAI) and high emission global warming (RCP8.5) scenarios compared to the current climate (CTL). Our results show that the future dust mass concentration would be reduced by up to 35% under both the RCP8.5 and SAI scenarios compared to the CTL, in the different areas of the MENA region. Although this reduction is slightly stronger
385   for the SAI simulations compared to RCP8.5 over the whole MENA region. However, a more detailed analysis of regions in the vicinity of dust hotspots in the summer of northeast Africa (R3) and the Middle East (R4 and R5), shows 5-15% more dust concentration under the SAI scenario compared to RCP8.5. Under the SAI simulations, the more densely

populated Middle East area would encounter more dust concentration (i.e., about 5-15%) than under the RCP8.5 scenario after 2060, but still, fewer (i.e., about 5-30%) dust concentration would occur compared to the present day. We further conclude that, over the coming 80 years, the dust mass concentration generally decreases under the both RCP8.5 and SAI scenarios with an increase in the precipitation, soil water, and leaf area index, and a decrease in 10m wind speed over the MENA region, particularly across the Middle East, and also over the dust hotspots, the near surface wind speed and precipitation have the most impact on this reduction.

Acknowledgments, Samples, and Data

Khalil Karami and Seyed Vahid Mousavi are partially supported by The World Academy of Sciences (TWAS) (grant no: A-097- FR3240304784). Lili Xia was supported by National Science Foundation grants AGS-2017113 and ENG-2028541.The CESM project is supported by the National Science. The data from the GLENS simulations is publicly available via its website: http://www.cesm.ucar.edu/projects/community-projects/GLENS/ (DOI: 10.5065/D6JH3JXX).

References

Albani, S., Mahowald, N. M., Perry, A. T., Scanza, R. A., Zender, C. S., Heavens, N. G., Maggi, V., Kok, J. F. and Otto Bliesner, B. L.: Improved dust representation in the Community Atmosphere Model, J. Adv. Model. Earth Syst., 6, 541–570, doi:10.1002/2013MS000279, 2014.

Albani, S., Balkanski, Y., Mahowald, N., Winckler, G., Maggi, V. and Delmonte, B.: Aerosol-Climate Interactions During the Last Glacial Maximum. Curr Clim Change Rep, 4(2), 99–114, doi:10.1007/s40641-018-0100-7, 2018.

Alboghdady, M., and El-Hendawy, S. E.: Economic impacts of climate change and variability on agricultural production in the Middle East and North Africa region. IJCCSM, 8(3), 463–472. doi:10.1108/ijccsm-07-2015-0100, 2016.

Alpert, P., Kaufman, Y., Shay-El, Y., Tanre, D., da Silva, A., Schubert, S. and Joseph, J. H.: Quantification of dust-forced heating of the lower troposphere, Nature 395, 367–370, doi:10.1038/26456, 1998.

Atkinson, J. D., Murray, B. J., Woodhouse, M. T., Whale, T. F., Baustian, K. J., Carslaw, K. S., Dobbie, S., O'Sullivan, D., and Malkin, T. L.: The importance of feldspar for ice nucleation by mineral dust in mixed-phase clouds. Nature, 498(7454), 355–358, doi:10.1038/nature12278, 2013.

Boucher, O., Randall, D., Artaxo, P., Bretherton, C., Feingold, G., Forster, P., Kerminen, VM., Kondo, Y., Liao, H., Lohmann, U., Rasch, P., Satheesh, SK., Sherwood, S., Stevens, B., Zhang, XY.: Clouds and aerosols, in: Climate change 2013: the physical science basis. Contribution of Working Group I to the Fifth Assessment Report of the Intergovernmental Panel on Climate Change, edited by: Stocker, T. F., Qin, D., Plattner, G.-K., Tignor, M., Allen, S. K., Boschung, J., Nauels, A., Xia, Y., Bex, V., and Midgley, P. M., Cambridge University Press, Cambridge, UK, 571–657, 2013.

Caldeira, K. and Matthews, H.D.: Transient climate-carbon simulations of planetary geoengineering, Proc Natl Acad Sci 104:9949–9954, doi:10.1073/pnas.0700419104, 2007.

420 Cao, J. J., Lee, S. C., Zhang, X. Y., Chow, J. C., An, Z. S., Ho, K. F., Watson, J. G., Fung, K., Wang, Y. Q., and Shen, Z. X.: Characterization of airborne carbonate over a site near Asian dust source regions during spring 2002 and its climatic and environmental significance, J. Geophys. Res., 110, D03203, doi:10.1029/2004JD005244, 2005.

Crutzen, P. J.: Albedo Enhancement by Stratospheric Sulfur Injections: A Contribution to Resolve a Policy Dilemma?, Clim. Change, 77, 211–219, doi:10.1007/s10584-006-9101-y, 2006.

425 Dufresne, J.-L., Gautier, C., Ricchiazzi, P., and Fouquart, Y.: Longwave Scattering Effects of Mineral Aerosols, J. Atmos. Sci., 59(12), 1959–1966, doi:10.1175/1520-0469(2002)059<1959:lseoma>2.0.co;2, 2002.

Gasso, S., Grassian, V. H., & Miller, R. L.: Interactions between Mineral Dust, Climate, and Ocean Ecosystems, Elements, 6(4), 247–252, doi:10.2113/gselements.6.4.247, 2010.

Giles, J.: The dustiest place on Earth, Nature, 434(7035), 816–819, doi:10.1038/434816a, 2005.

430 Ginoux, P., Prospero, J. M., Gill, T. E., Hsu, N. C., and Zhao, M.: Global-scale attribution of anthropogenic and natural dust sources and their emission rates based on MODIS Deep Blue aerosol products, Rev. Geophys., 50, RG3005, doi:10.1029/2012RG000388, 2012.

Giorgi, F., Coppola, E., Solmon, F., Mariotti, L., Sylla, MB., Bi, XQ., Elguindi, N., Diro, GT., Nair, V., Giuliani, G., Turuncoglu, UU., Cozzini, S., Güttler, I., O'Brien, TA., Tawfik, AB., Shalaby, A., Zakey, AS., Steiner, AL., Stordal, F.,
435 Sloan, LC., Brankovic, C.: RegCM4: model description and preliminary tests over multiple CORDEX domains. Clim Res 52:7–29, doi:10.3354/cr01018, 2012.

Hillel, D.: Introduction to Soil Physics, Academic, San Diego, Calif., 1982.

Holman, I.P., Rivas-Casado, M., Howden, N.J.K., Bloomfield, J.P., Williams, A.T.: Linking North Atlantic ocean-atmosphere teleconnection patterns and hydrogeological responses in temperate groundwater systems. Hydrological
440 Processes, 23. 3123-3126, doi:10.1002/hyp.7466, 2009.

Huneeus, N., Schulz, M., Balkanski, Y., Griesfeller, J., Prospero, J., Kinne, S., Bauer, S., Boucher, O., Chin, M., Dentener, F., Diehl, T., Easter, R., Fillmore, D., Ghan, S., Ginoux, P., Grini, A., Horowitz, L., Koch, D., Krol, M. C., Landing, W., Hurrell, J. W., and Holland, M. M., Gent, P. R., Ghan, S., Kay, Jennifer E., Kushner, P. J., Lamarque, J.-F., Large, W. G., Lawrence, D., Lindsay, K., Lipscomb, W. H., Long, M. C., Mahowald, N., Marsh, D. R., Neale, R. B., Rasch, P., Vavrus,
445 S., Vertenstein, M., Bader, D., Collins, W. D., Hack, J. J., Kiehl, J., and Marshall, S.: The Community Earth System Model: A framework for collaborative research. Bull. Amer. Meteor. Soc., 94, 1339–1360, doi:10.1175/BAMS-D-12-00121.1., 2013.

Jickells, T. D.: Global Iron Connections Between Desert Dust, Ocean Biogeochemistry, and Climate, Science, 308(5718), 67–71, doi:10.1126/science.1105959, 2005.

450 Ji, Z., Wang, G., Yu, M., and Pal, J. S.: Potential climate effect of mineral aerosols over West Africa: Part II—contribution of dust and land cover to future climate change. Clim Dyn 50, 2335–2353, doi:10.1007/s00382-015-2792-x, 2018.

Karami, K., Tilmes, S., Muri, H., and Mousavi, S. V.: Storm track changes in the Middle East and North Africa under stratospheric aerosol geoengineering. Geophysical Research Letters, 47, e2020GL086954, doi:10.1029/2020GL086954, 2020.

455 Karami, K. (2019). Upper tropospheric Rossby wave packets: long-term trends and variability. *Theoretical and Applied Climatology*, *138*(1), 527-540.

Keith, D., Weisenstein, D., Visioni, D., Franke, H.: GeoMIP Test Bed Experiment: Injection of Accumulation Mode H2SO4 Particles in Chemistry-Climate Models, American Geophysical Union, Fall Meeting 2019,

Kok, J. F., Ridley, D. A., Zhou, Q., Miller, R. L., Zhao, C., Heald, C. L., Ward, D. S., Albani, S., Haustein, K.: Smaller
460 desert dust cooling effect estimated from analysis of dust size and abundance, Nature Geosci, 10(4), 274–278, doi:10.1038/ngeo2912, 2017.

Kok, J. F., Albani, S., Mahowald, N. M., and Ward, D. S.: An improved dust emission model – Part 2: Evaluation in the Community Earth System Model, with implications for the use of dust source functions, Atmos. Chem. Phys., 14, 13043–13061, doi:10.5194/acp-14-13043-2014, 2014.

465 Kok, J. F., Ward, D. S., Mahowald, N. M., & Evan, A. T.: Global and regional importance of the direct dust-climate feedback. Nat Commun 9, 241, doi:10.1038/s41467-017-02620-y, 2018.

Kravitz, B., MacMartin, D. G., Mills, M. J., Richter, J. H., Tilmes, S., Lamarque, J.-F., Tribbia, J. J, Vitt, F.: First Simulations of Designing Stratospheric Sulfate Aerosol Geoengineering to Meet Multiple Simultaneous Climate Objectives, J. Geophys. Res.-Atmos., 122(23), 12,616–12,634, doi:10.1002/2017jd026874, 2017.

470 Krinner, G., Boucher, O., & Balkanski, Y.: Ice-free glacial northern Asia due to dust deposition on snow. Clim. Dyn., 27(6), 613–625, doi:10.1007/s00382-006-0159-z, 2006.

Lomborg, B.: Impact of Current Climate Proposals. Glob Policy, 7: 109-118, doi:10.1111/1758-5899.12295, 2016.

Liu, J., Wu, D., Liu, G., Mao, R., Chen, S., Ji, M., Fu, P., Sun, Y., Pan, X., Jin, H., Zhou, Y., Wang, X..: Impact of Arctic amplification on declining spring dust events in East Asia. Climate Dynamics, doi:10.1007/s00382-019-05094-4, 2019.

475 Liu, X., Easter, R. C., Ghan, S. J., Zaveri, R., Rasch, P., Shi, X., Lamarque, J.-F., Gettelman, A., Morrison, H., Vitt, F., Conley, A., Park, S., Neale, R., Hannay, C., Ekman, A. M. L., Hess, P., Mahowald, N., Collins, W., Iacono, M. J., Bretherton, C. S., Flanner, M. G., Mitchell, D.: Toward a minimal representation of aerosols in climate models: description and evaluation in the Community Atmosphere Model CAM5. Geoscientific Model Development, 5(3), 709–739, doi:10.5194/gmd-5-709-2012, 2012.

480 Liu, X., Mahowald, N., Miller, R., Morcrette, J.-J., Myhre, G., Penner, J., Perlwitz, J., Stier, P., Takemura, T., and Zender, C. S.: Global dust model intercomparison in AeroCom phase I, Atmos. Chem. Phys., 11, 7781–7816, doi:10.5194/acp-11-7781-2011, 2011.

Macnaghten, P., Szerszynski, B.: Living the global social experiment: An analysis of public discourse on solar radiation management and its implications for governance, Global Environmental Change, 465-474,
485 doi:10.1016/j.gloenvcha.2012.12.008, 2013.

MacMartin, D. G., Wang, W., Kravitz, B., Tilmes, S., Richter, J. H., & Mills, M. J.: Timescale for detecting the climate response to stratospheric aerosol geoengineering. Journal of Geophysical Research: Atmospheres, 124, doi:10.1029/2018JD028906, 2017.

490   Mahowald, N., Albani, S., Kok, J. F., Engelstaeder, S., Scanza, R., Ward, D. S., & Flanner, M. G.: The size distribution of desert dust aerosols and its impact on the Earth system. Aeolian Research, 15, 53–71, doi:10.1016/j.aeolia.2013.09.002, 2014.

Mahowald, N., Kohfeld, K., Hansson, M., Balkanski, Y., Harrison, S. P., Printice, I. C., Schulz, M., and Rodhe, H.: Dust sources and deposition during the last glacial maximum and current climate: A comparison of model results with paleodata from ice cores and marine sediments, J. Geophys. Res., 104, 15,895– 15,916, doi:10.1029/1999JD900084, 1999.

495   Mahowald, N. M., and Luo, C.: A less dusty future? Geophys. Res. Lett., 30, 1903, doi:10.1029/2003GL017880, 17, 2003.

Mahowald, N. M., Kloster, S., Engelstaedter, S., Moore, J. K., Mukhopadhyay, S., McConnell, J. R., Albani, S., Doney, S. C., Bhattacharya, A., Curran, M. A. J., Flanner, M. G., Hoffman, F. M., Lawrence, D. M., Lindsay, K., Mayewski, P. A., Neff, J., Rothenberg, D., Thomas, E., Thornton, P. E., and Zender, C. S.: Observed 20th century desert dust variability: impact on climate and biogeochemistry, Atmos. Chem. Phys., 10, 10875–10893, doi:10.5194/acp-10-10875-2010, 2010.

500   Mahowald, N. M., Muhs, D. R., Levis, S., Rasch, P. J., Yoshioka, M., Zender, C. S., and C. Luo: Change in atmospheric mineral aerosols in response to climate: Last glacial period, preindustrial, modern, and doubled carbon dioxide climates, J. Geophys. Res., 111, D10202, doi:10.1029/2005JD006653, 2006.

Marsh, D. R., Mills, M. J., Kinnison, D. E., Lamarque J.-F., Calvo N., and Polvani L. M.: Climate change from 1850 to 2005 simulated in CESM1(WACCM). J. Climate, 26, 7372–7391, doi: /10.1175/JCLI-D-12-00558.1, 2013.

505   McClellan, J., Sisco, J., Suarez, B., Keogh, G.: Geoengineering cost analysis. Final report, Aurora Flight Sciences Corporation, Cambridge, Massachusetts, 2010.

Middleton, N. J.: Desert dust hazards: A global review. Aeolian Research, 24, 53–63, doi:10.1016/j.aeolia.2016.12.001, 2017.

Millar, R.J., Fuglestvedt, J.S., Friedlingstein, P., Rogelj, J., Grubb, M.J., Matthews, H.D., Skeie, R.B., Forster, P.M.,
510   Frame, D.J. and Allen, M.R.: Emission budgets and pathways consistent with limiting warming to 1.5 °C. Nature Geosci 10, 741–747, doi:10.1038/ngeo3031, 2017.

Mills, M. J., Richter, J. H., Tilmes, S., Kravitz, B., MacMartin, D. G., Glanville, A. A., Tribbia, J. J., Lamarque, J. F., Vitt, F., Schmidt, A., Gettelman, A., Hannay, C., Bacmeister, J. T., and Kinnison, D. E.: Radiative and Chemical Response to Interactive Stratospheric Sulfate Aerosols in Fully Coupled CESM1(WACCM), J. Geophys. Res.-Atmos., 122, 13061–
515   13078, doi:10.1002/2017JD027006, 2017.

Mills, M. J., Schmidt, A., Easter, R., Solomon, S., Kinnison, D. E., Ghan, S. J., Neely, R. R., Marsh, D. R., Conley, A., Bardeen, Ch. G., Gettelman, A.: Global volcanic aerosol properties derived from emissions, 1990–2014, using CESM1(WACCM), J. Geophys. Res. Atmos., 121, 2332–2348, doi:10.1002/2015JD024290, 2016.

Nicholson, S. E., C. J. Tucker, and M. B. Ba, Desertification, drought, and surface vegetation: An example from the West African Sahel, Bull. Am. Meteorol. Soc., 79, 815–829, doi:10.1175/1520-0477, 1998.

Nurse, P.: I hope we never need geoengineering, but we must research it. The Guardian 08 September. Retrieved February 9, 2020, from http://www.guardian.co.uk/environment/ 2011/sep/08/geoengineering-research-royal-society, 2011.

Oleson, K., Lawrence, D. M., Bonan, G. B., Drewniak, B., Huang, M., Koven, C. D., Levis, S., Li, F., Riley, J. P., Subin, M. Ch., Swenson, S. C., Thornton, E., Bozbiyik, A., Fisher, R. A., Heald, L., Kluzek, E., Lamarque, J. F., Lawrence, J., Leung, R., Lipscomb, W. H., Muszala, P., Ricciuto, M., Sacks, J., Sun, Y., Tang, J., Yang, Z. L.: Technical description of version 4.5 of the Community Land Model (CLM) (No. NCAR/TN-503+STR). doi:10.5065/D6RR1W7M, 2013.

Orlovsky L., Orlovsky N., Durdyev A.: Dust storms in Turkmenistan, 60(1), 0–97, doi:10.1016/j.jaridenv.2004.02.008, 2005.

Painter, T. H., Flanner, M. G., Kaser, G., Marzeion, B., VanCuren, R. A., & Abdalati, W.: End of the Little Ice Age in the Alps forced by industrial black carbon, Proc Natl Acad Sci, 110(38), 15216–15221, doi:10.1073/pnas.1302570110, 2013.

Pasztor, J., Turner, M.: Optimism and prudence in geoengineering governance, Carnegie Climate Geoengineering Governance Initiative. https://www.c2g2.net/optimism-vs-prudence-geo-governance, 2018.

Prospero, J. M.: Environmental characterization of global sources of atmospheric soil dust identified with the NIMBUS 7 Total Ozone Mapping Spectrometer (TOMS) absorbing aerosol product, Rev. Geophys., 40(1), doi:10.1029/2000rg000095, 2002.

Rasch, P.J., Tilmes, S., Turco, R., Robock, A., Oman, L., Chen, C-C, Stenchikov, G., Garcia, R., An overview of geoengineering of climate using stratospheric sulphate aerosols. 366. Phil. Trans. R. Soc. A: Mathematical, Physical and Engineering Sciences, doi:10.1098/rsta.2008.0131, 2008.

Raupach, M.R. Simplified expressions for vegetation roughness length and zero-plane displacement as functions of canopy height and area index. Boundary-Layer Meteorol 71, 211–216, doi:10.1007/BF00709229, 1994.

Robock, A. (2008). 20 reasons why geoengineering may be a bad idea, Bull. At. Sci., 64(2), 14–18, doi:10.2968/064002006, 2008.

Rozenberg, J., Davis, S. J., Narloch, U., Hallegatte, S.: Climate constraints on the carbon intensity of economic growth, Environ. Res. Lett., 10(9), 095006, doi:10.1088/1748-9326/10/9/095006, 2015.

Sagoo, N., & Storelvmo, T.: Testing the sensitivity of past climates to the indirect effects of dust, Geophys. Res. Lett, 44(11), 5807–5817, doi:10.1002/2017gl072584, 2017.

Sanderson, M-B., O'Neill, B., Tebaldi, B.: What would it take to achieve the Paris temperature targets?, Geophys. Res. Lett, doi:10.1002/2016GL069563, 2016.

Sarangi, C., Qian, Y., Rittger, K., Leung, L.R., Chand, D., Bormann, K.J. and Painter, T.H.: Dust dominates high-altitude snow darkening and melt over high-mountain Asia. Nature Climate Change, pp.1-7, doi:10.1038/s41558-020-00909-3, 2020.

Seneviratne, S. I., Corti, T., Davin, E. L., Hirschi, M., Jaeger, E. B., Lehner, I., Orlowsky, B., Teuling, A. J.: Investigating soil moisture–climate interactions in a changing climate: A review, Earth-Science Reviews, Volume 99, Issues 3–4, Pages 125-161, doi:10.1016/j.earscirev.2010.02.004, 2010.

555 Simpson, I. R., Tilmes, S., Richter, J. H., Kravitz, B., MacMartin, D. G., Mills, M. J., …: The regional hydroclimate response to stratospheric sulfate geoengineering and the role of stratospheric heating, Journal of Geophysical Research: Atmospheres, doi:10.1029/2019jd031093, 2019.

Sternberg, T., & Edwards, M.: Desert Dust and Health: A Central Asian Review and Steppe Case Study, IJERPH, 14(11), 1342 doi:10.3390/ijerph14111342, 2017.

560 Tegen, I., Harrison, S. P., Kohfeld, K., Prentice, I. C., Coe, M., & Heimann, M.: Impact of vegetation and preferential source areas on global dust aerosol: results from a model study. J. Geophys. Res., 107(21), 1-36, 4576, doi:10.1029/2001JD000963, 2002.

Tegen, Ina, and Inez Fung.: Modeling of mineral dust in the atmosphere: Sources, transport, and optical thickness. Journal of Geophysical Research: Atmospheres 99.D11 (1994): 22897-22914, doi: 10.1029/94JD01928, 1994.

565 Tegen, I., Werner, M., Harrison, S. P., and Kohfeld, K. E.: Relative importance of climate and land use in determining present and future global soil dust emission, Geophys. Res. Lett., 31, L05105, doi:10.1029/2003GL019216, 2004.

Textor, C., Schulz, M., Guibert, S., Kinne, S., Balkanski, Y., Bauer, S., Berntsen, T., Berglen, T., Boucher, O., Chin, M., Dentener, F., Diehl, T., Easter, R., Feichter, H., Fillmore, D., Ghan, S., Ginoux, P., Gong, S., Grini, A., Hendricks, J., Horowitz, L., Huang, P., Isaksen, I., Iversen, I., Kloster, S., Koch, D., Kirkevåg, A., Kristjansson, J. E., Krol, M., Lauer,

570 A., Lamarque, J. F., Liu, X., Montanaro, V., Myhre, G., Penner, J., Pitari, G., Reddy, S., Seland, Ø., Stier, P., Takemura, T., and Tie, X.: Analysis and quantification of the diversities of aerosol life cycles within AeroCom, Atmos. Chem. Phys., 6, 1777–1813, doi:10.5194/acp-6-1777-2006, 2006.

Tilmes, S., Richter, J. H., Kravitz, B., MacMartin, D. G., Mills, M. J., Simpson, I. R., . . . Ghosh, S.: CESMI (WACCM) stratospheric aerosol geoengineering large ensemble project, Bull. Am. Meteorol. Soc., 99(11), 2361-2371,

575 doi:10.1175/bams-d-17-0267.1, 2018.

Ueyama, M., Ichii, K., Kobayashi, H., Kumagai, T., Beringer, J., Merbold, L., … Yasuda, Y.: Inferring CO_2 fertilization effect based on global monitoring land-atmosphere exchange with a theoretical model. Environmental Research Letters. doi:10.1088/1748-9326/ab79e5, 2020.

Vattioni, S., Weisenstein, D., Keith, D., Feinberg, A., Peter, T., and Stenke, A.: Exploring accumulation-mode H_2SO_4

580 versus SO_2 stratospheric sulfate geoengineering in a sectional aerosol–chemistry–climate model, Atmos. Chem. Phys., 19, 4877–4897, doi:10.5194/acp-19-4877-2019, 2019.

Visioni, D., MacMartin, D. G., Kravitz, B., Richter, J. H., Tilmes, S., & Mills, M. J., Seasonally modulated stratospheric aerosol geoengineering alters the climate outcomes, Geophysical Research Letters, 47, e2020GL088337., doi:10.1029/2020GL088337, 2020.

585   Wang, F., Zhao, X., Gerlein-Safdi, C., Mu, Y., Wang, D., & Lu, Q.: Global sources, emissions, transport and deposition of dust and sand and their effects on the climate and environment: a review Front. Environ. Sci. Eng., 11(1), doi:10.1007/s11783-017-0904-z, 2017

Wang, W., Lee, X., Xiao, W. et al.: Global lake evaporation accelerated by changes in surface energy allocation in a warmer climate. Nature Geosci 11, 410–414, doi:10.1038/s41561-018-0114-8, 2018.

590   WMO, UNEP. 2013. Establishing a WMO sand and dust storm warning advisory and assessment system regional node for West Asia: current capabilities and needs. In: WMO Technical Report, 1121.

Woodward, S., Roberts, D. L., & Betts, R. A.: A simulation of the effect of climate change-induced desertification on mineral dust aerosol, Geophys. Res. Lett, 32(18), n/a–n/a, doi:10.1029/2005gl023482, 2005.

Wu, C., Lin, Z., and Liu, X.: The global dust cycle and uncertainty in CMIP5 (Coupled Model Intercomparison Project

595   phase 5) models, Atmos. Chem. Phys., 20, 10401–10425, doi:10.5194/acp-20-10401-2020, 2020.

Yue, X., Wang, H., Liao, H., and Fan, K.: Simulation of dust aerosol radiative feedback using the GMOD: 2, Dust-climate interactions, J. Geophys. Res., 115, D04201, doi:10.1029/2009jd012063, 2010.

Žagar, N., et al. (2020). Atmospheric Subseasonal Variability and Circulation Regimes: Spectra, Trends, and Uncertainties, *Journal of Climate*, *33*(21), 9375-9390.

600   Zender, C.S., Bian, H., and Newman, D.: Mineral dust entrainment and deposition (DEAD) model: Description and 1990s dust climatology. J. Geophys. Res., VOL. 108, NO. D14, 4416, doi:10.1029/2002JD002775, 2003

Table 1. Component of the ECSM1 used in GLENS project

Component	Version	Reference
Atmosphere	WACCM	Marsh et al. (2013), Mills et al. (2017)
Aerosol	MAM3	Liu et al. (2012), Mills et al., 2016
Land	CLM4.5	Oleson et al. (2013)

605

Table 2. Number of ensembles for each simulation

Simulation	Acronym	Period	Number of Ensembles
current climate simulation	CTL	2010 – 2029	20
future climate simulation	RCP	2078 – 2097	3
feedback simulation	SAI	2078 – 2097	20

610

Table 3. The correlation coefficient of dust with considered parameters for all dust hotspots over the MEAN region. The most important variables for each region highlighted by orange color. The correlation coefficients are calculated using detrended annual mean time series resulting from the average of all ensemble members, and spatially averaged over
615 **the corresponding dust hotspot region.**

	RCP8.5 Scenario (2020-2097)					SAI Scenario (2020-2099)				
	R1	R2	R3	R4	R5	R1	R2	R3	R4	R5
Wind Speed	0.70	0.64	0.66	0.37	0.27	0.70	0.50	0.71	0.39	0.35
Precipitation	-0.31	-0.15	-0.18	-0.35	-0.28	-0.24	-0.23	-0.13	-0.34	-0.27
Soil Water	-0.10	-0.18	-0.04	-0.24	-0.16	-0.04	-0.29	0.06	-0.26	-0.26
Leaf Are Index	-0.10	-0.18	-0.02	-0.01	-0.16	-0.25	-0.31	-0.04	-0.01	-0.14
Surface Temperature	-0.36	0.22	-0.24	-0.13	-0.03	-0.11	0.08	-0.16	-0.10	-0.03
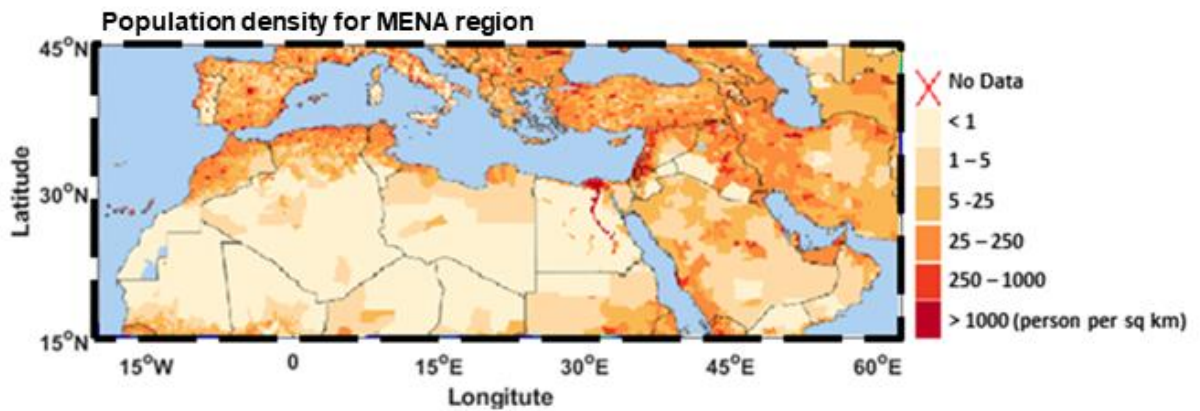
620 **Figure 1: Population density in the MENA region [(SEDECA: https://sedac.ciesin.columbia.edu/).].**
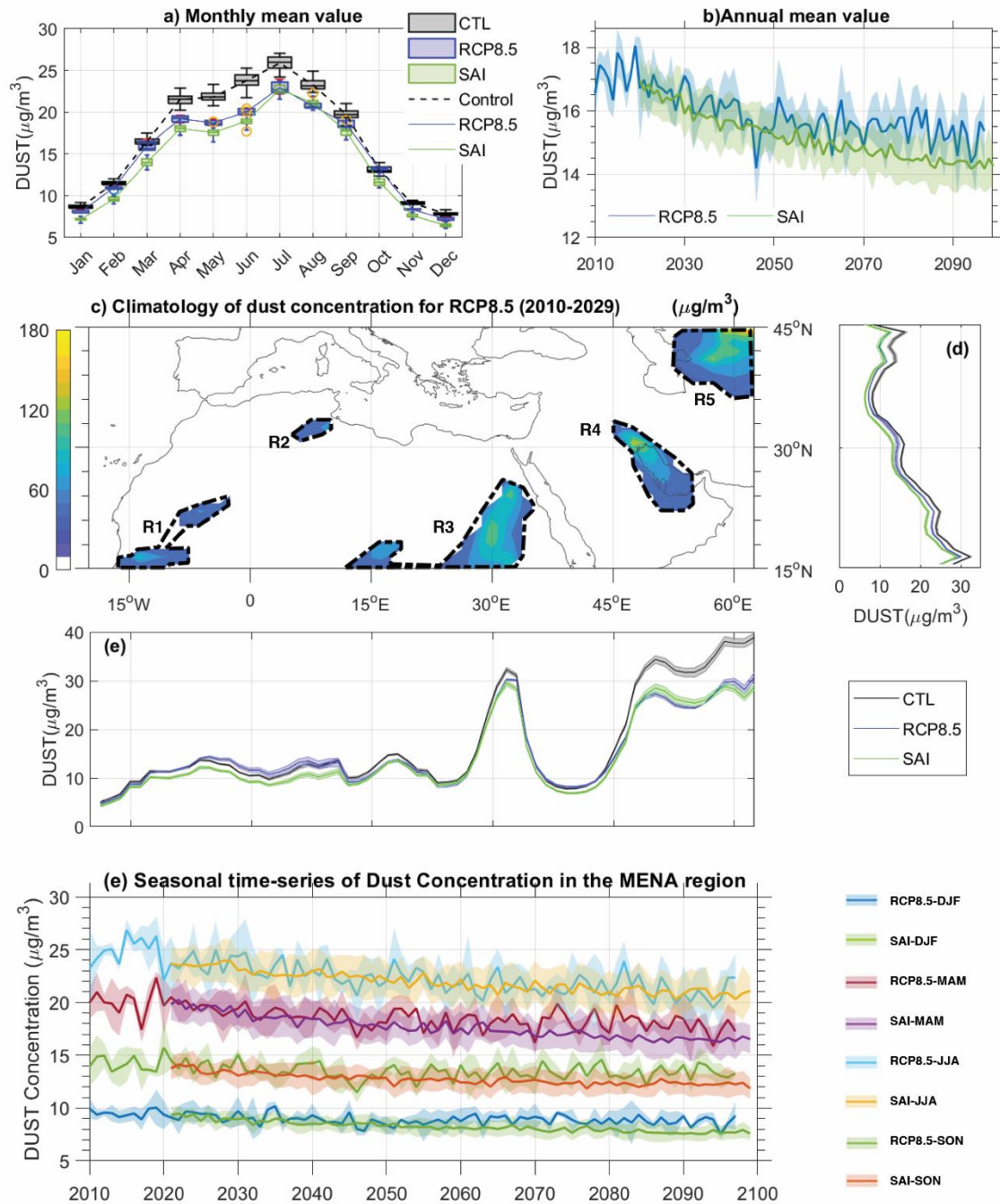
Figure 2: The monthly (a) and annual (b) mean values of the dust concentration for different scenarios, The box plots in (a) are depicted with the median (horizontal line), the 25–75 percentile (box), the 5–95 percentile (horizontal line), and outlier data (circle), and the shaded region in (b) indicated the standard deviation of all available ensemble members. c) Climatology of dust concentration of RCP8.5 (2010-2029), mean values are calculated for all available ensemble member in the GLENS dataset. In (c), black dash-line contours show the dust concentration hotspots. Mean values over different latitude (d) and different longitude (e) of annual dust concentration and their standard deviation in the MENA region of CTL (2010-2029), RCP8.5 and SAI (2010-2029). f) The seasonal mean dust concentration in the MENA region under SAI and RCP8.5 simulations.
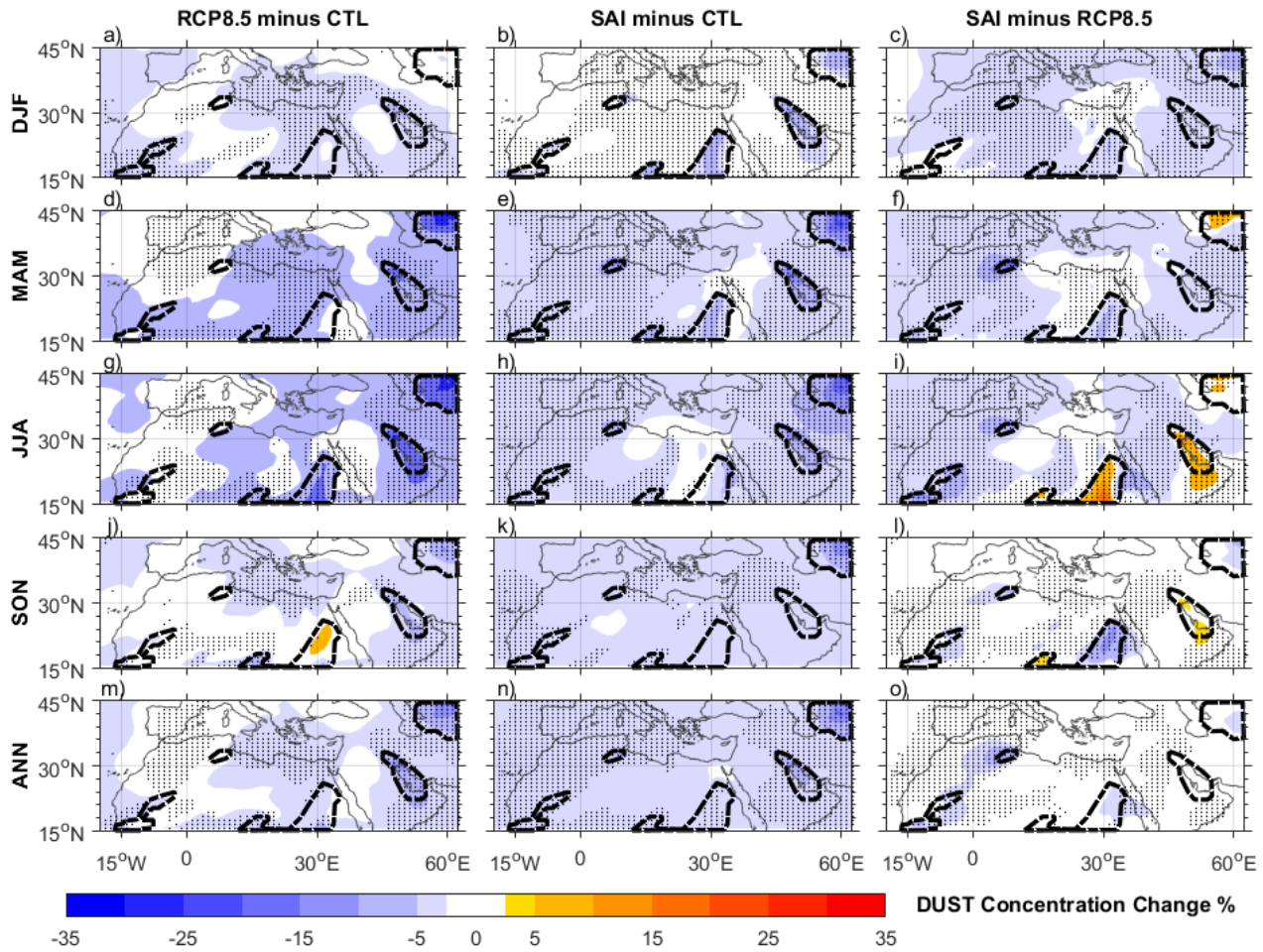
Figure 3: (a-o) Seasonal and annual percent of changes of dust mass concentration mean value in the MENA region under different climate scenarios. All available ensemble members of the GLENS project are used to calculate mean value of dust concentration for CTL (2010-2029), RCP8.5 (2078-2097) and SAI (2078-2097). The dashed line contours show dust hotspots and the regions with hatch line shows student's t-test analysis with 99.9% significance level. The percent of changes has been calculated relative to the maximum value of dust concentration in the CTL scenario over the whole MENA region (i.e., 185.75 $\mu g/m^3$).
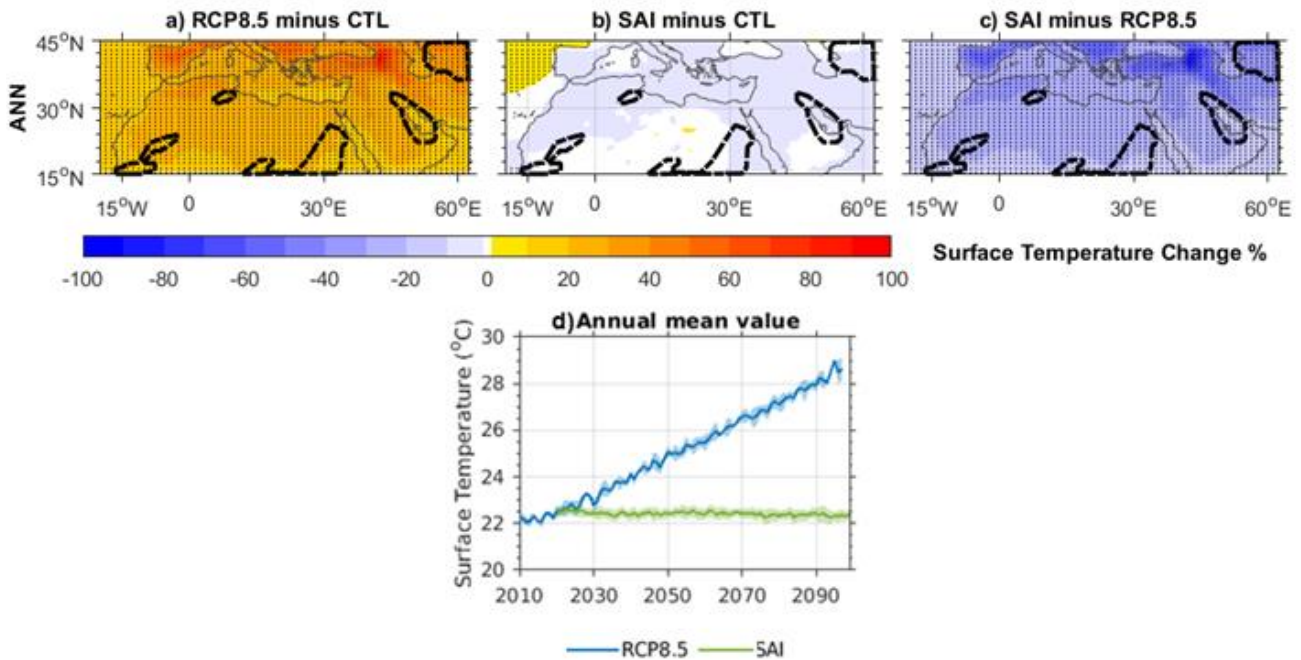
640

Figure 4: Annual changes of surface temperature mean value in the MENA region under different climate scenarios (a - c). All available ensemble members of the GLENS project are used to calculate mean value of surface temperature for CTL (2010-2029), RCP8.5 (2078-2097) and SAI (2078-2097). The percentage of change has been calculated relative to the current climate (CTL scenario). The dashed line contours show dust hotspots and the regions without hatch line shows student's t-test analysis

645 **with 99.9% significance level. d) The annual mean values of the surface temperature for different scenarios are shown, shaded envelope in (d) show standard deviation of annual surface temperature for RCP8.5 and SAI scenarios.**
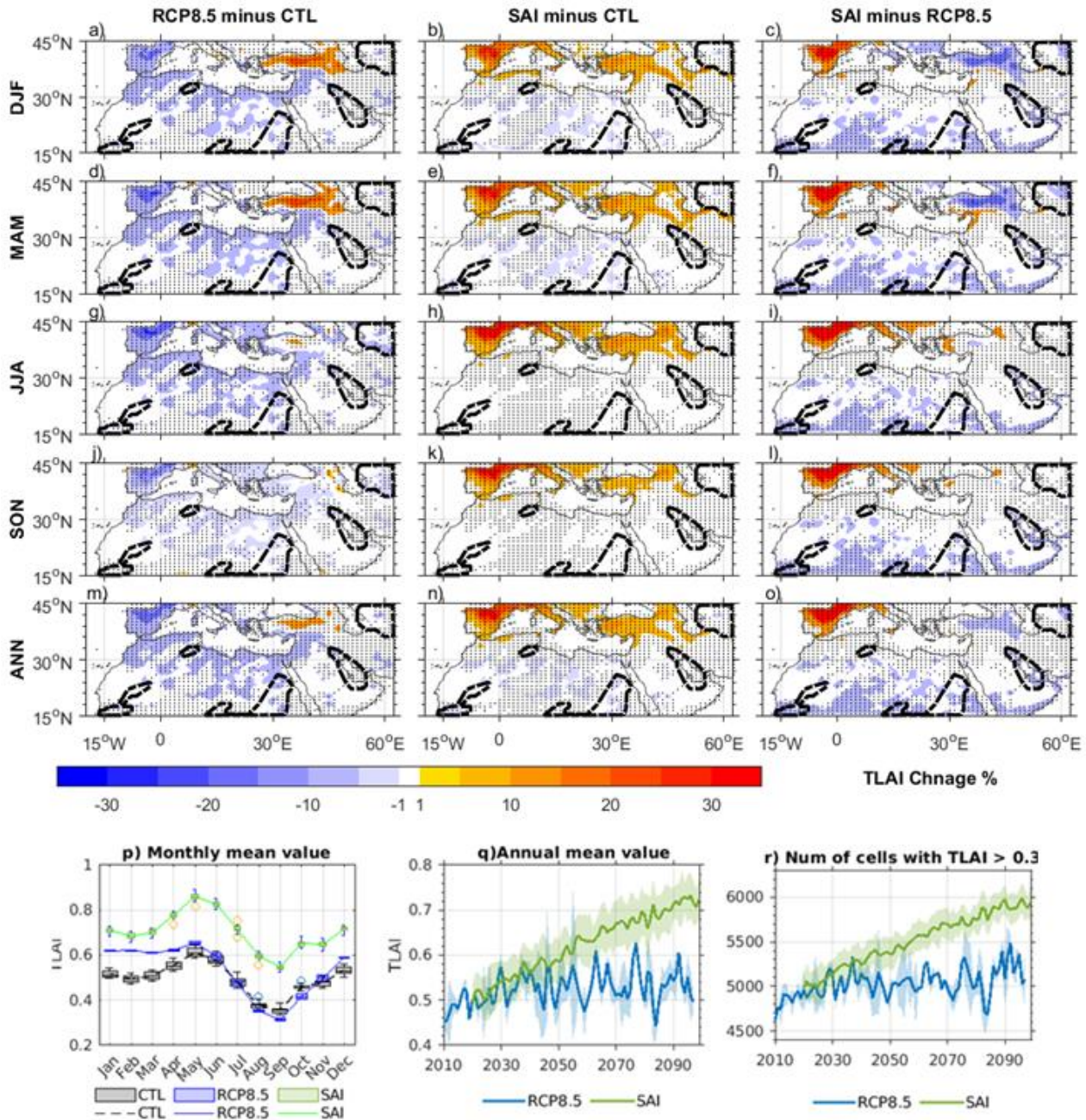
Figure 5: The same as Fig 3 but for the total leaf area index (TLAI) differences (TLAI is a unitless parameter). The percent of changes for total leaf are index has been calculated relative to the maximum value of TLAI in the CTL scenario over the whole MENA region ($TLAI_{MAX} = 7.33$). The monthly mean values of the TLAI for different scenarios (p). The box plots in (p) are depicted with the median (horizontal line), the 25–75 percentile (box), the 5–95 percentile (horizontal line), and outlier data (circle). Fig. 6q shows the annual mean value with its standard deviation (indicated by the shaded region) of TLAI for different scenarios. r) The time series of the annual mean total leaf area index higher than 0.3 (that is considered as minimum threshold for the dust emission) in the MENA region.
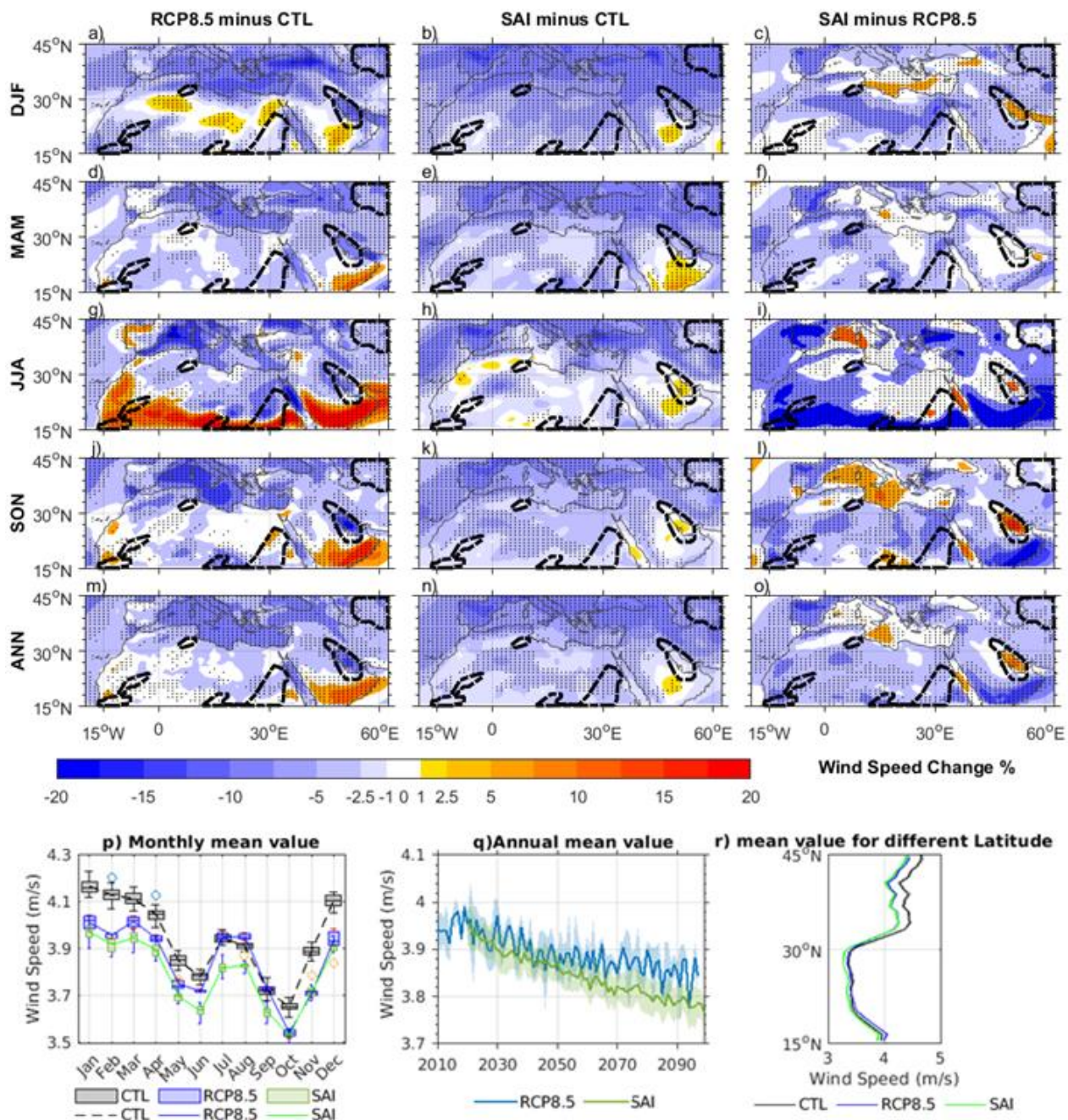
Figure 6: The same as Fig 5 but for the wind speed differences. The percentage of change has been calculated relative to the current climate (CTL scenario). r) is mean value of annual wind speed over different latitude with its standard deviation for MENA region.

660
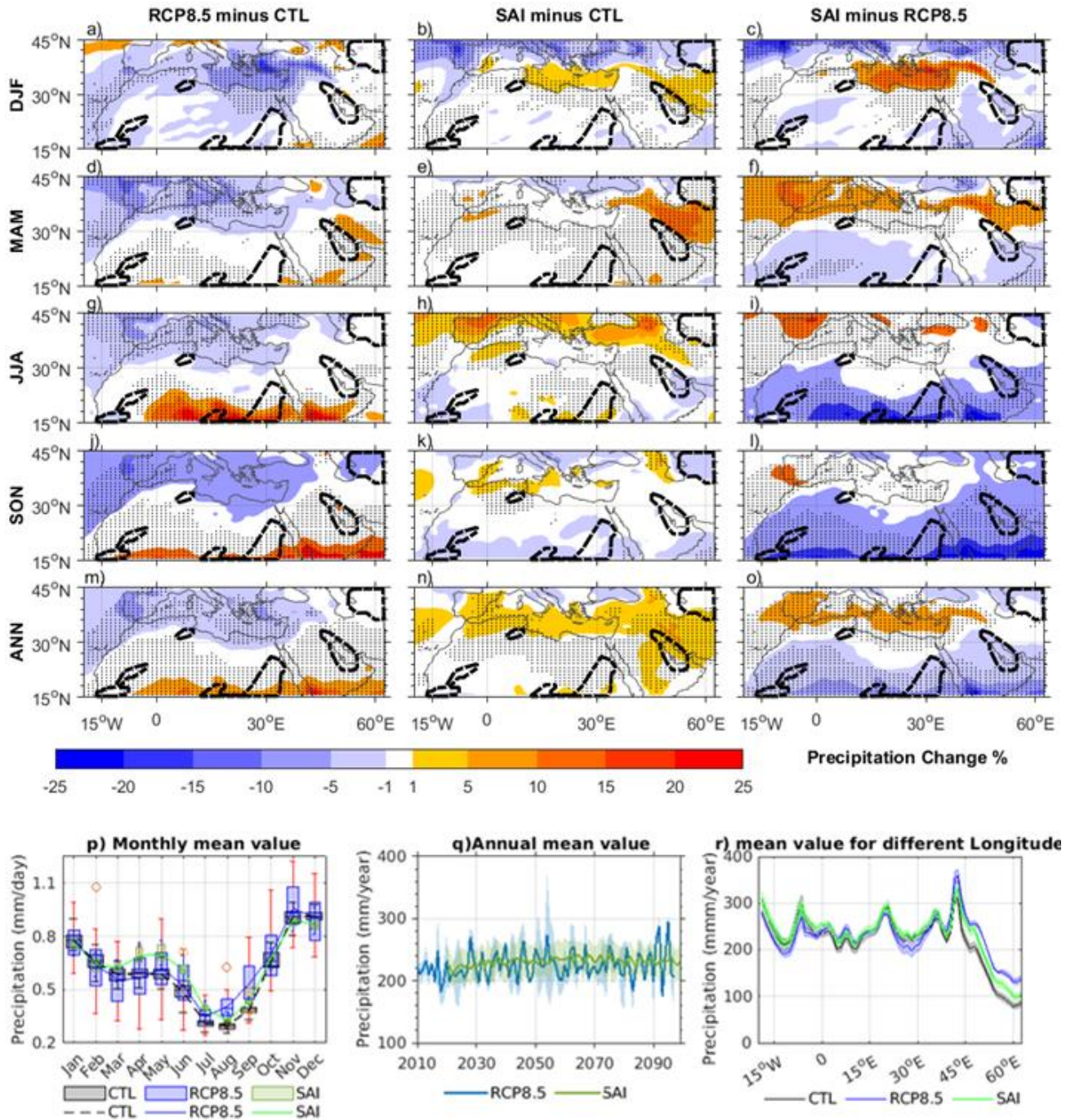
Figure 7: The same as Fig 5 but for the precipitation. The percent of changes for precipitation has been calculated relative to
665 **the maximum value of precipitation in the CTL scenario over the whole MENA region ($Precipitation_{MAX}$= 4.70 (mm/day)).**
r) Is mean value of annual precipitation over different longitude with its standard deviation for MENA region.
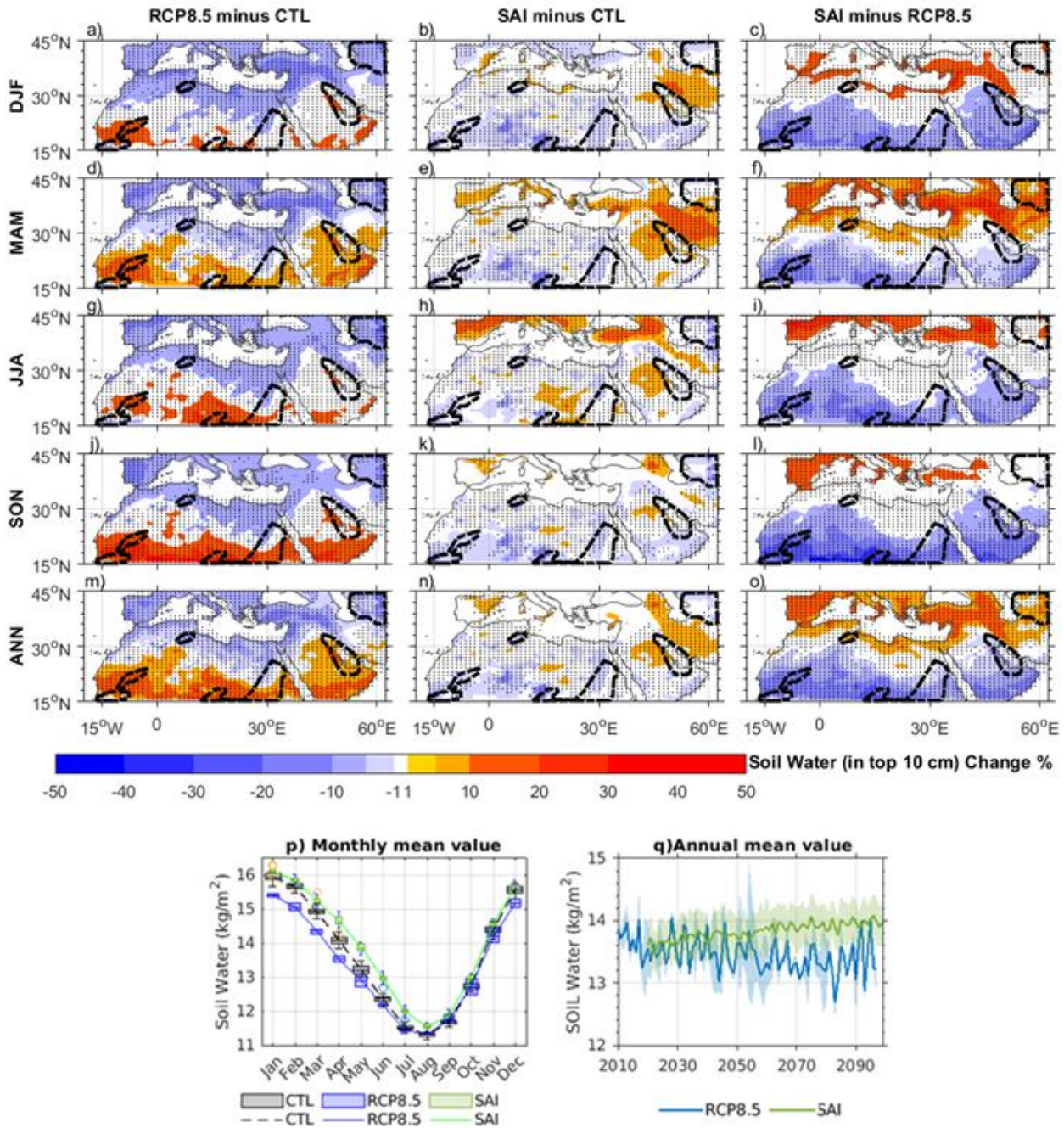
670

Figure 8: The same as Fig 5 but for the top 10 cm soil water. The percentage of change has been calculated relative to the current climate (CTL scenario).
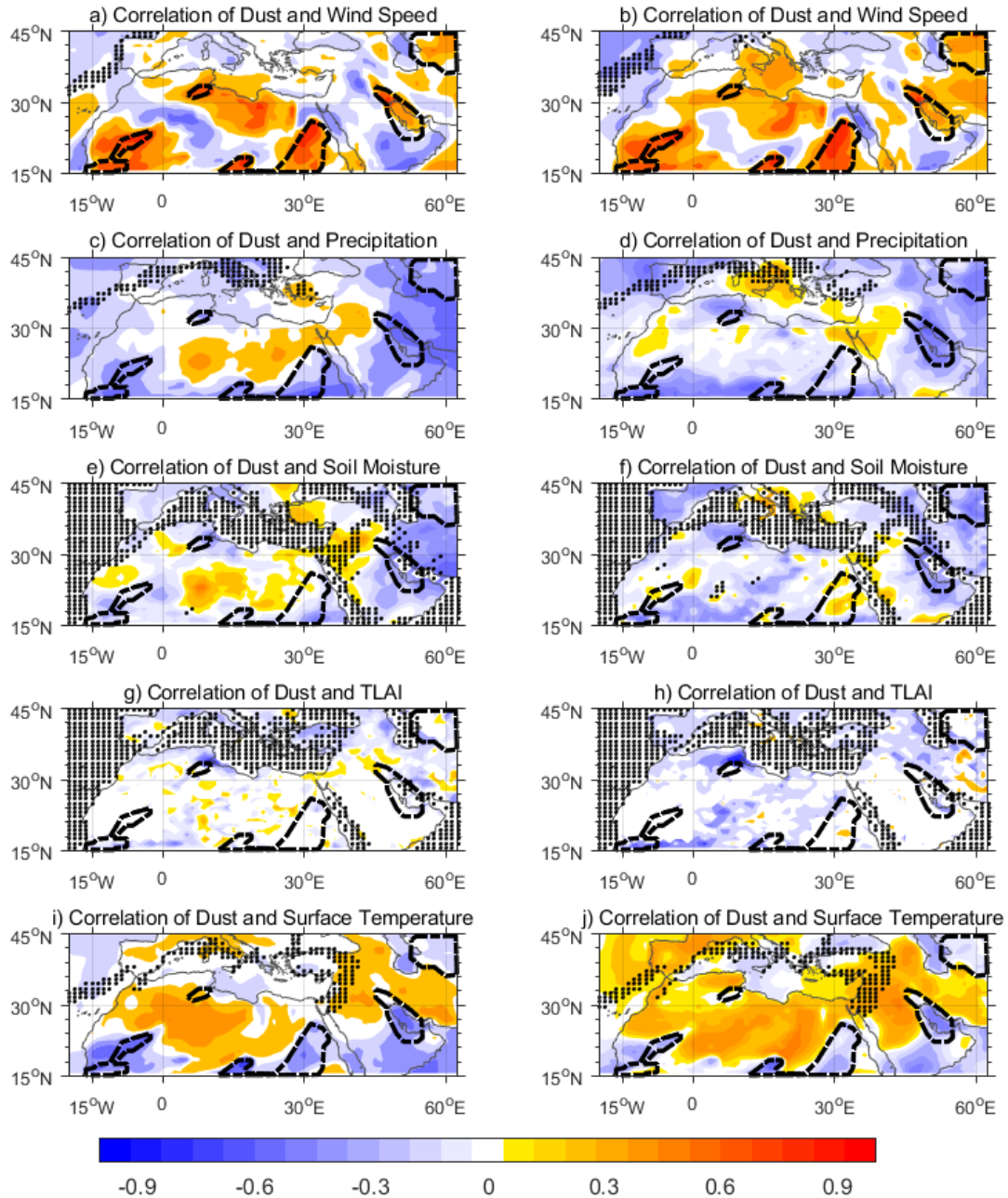
675

Figure 9: the correlation coefficient of dust with other considered parameters for all grids (i.e., cells with a horizontal resolution of 0.9° latitude by 1.25° longitude) over the MEAN region. The correlation is calculated using the detrended annual mean time series of all grids. The dashed line contours show dust hotspots (R1 to R5) regions. Furthermore, the regions without hatch line show statistically significance region with 99.5% confidence level.

680
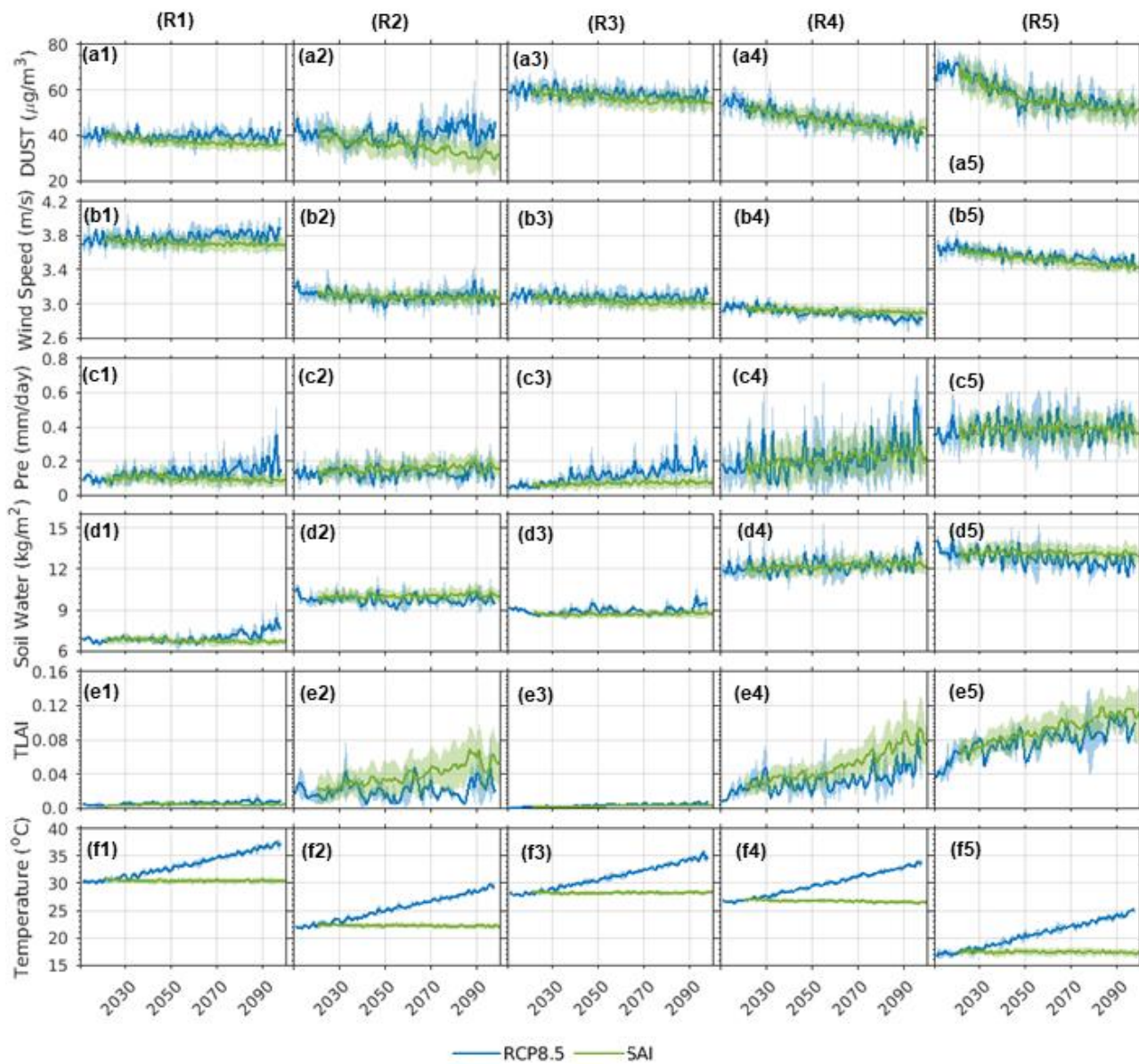
Figure 10: The annual mean values of the considered parameters for RCP8.5 and SAI scenarios. Different columns (i.e., columns 1 to 5) indicates the dust hotspots region R1 to R5, respectively, and different rows depicted the annual mean trends for different parameters with their standard deviation for all ensemble members.

685
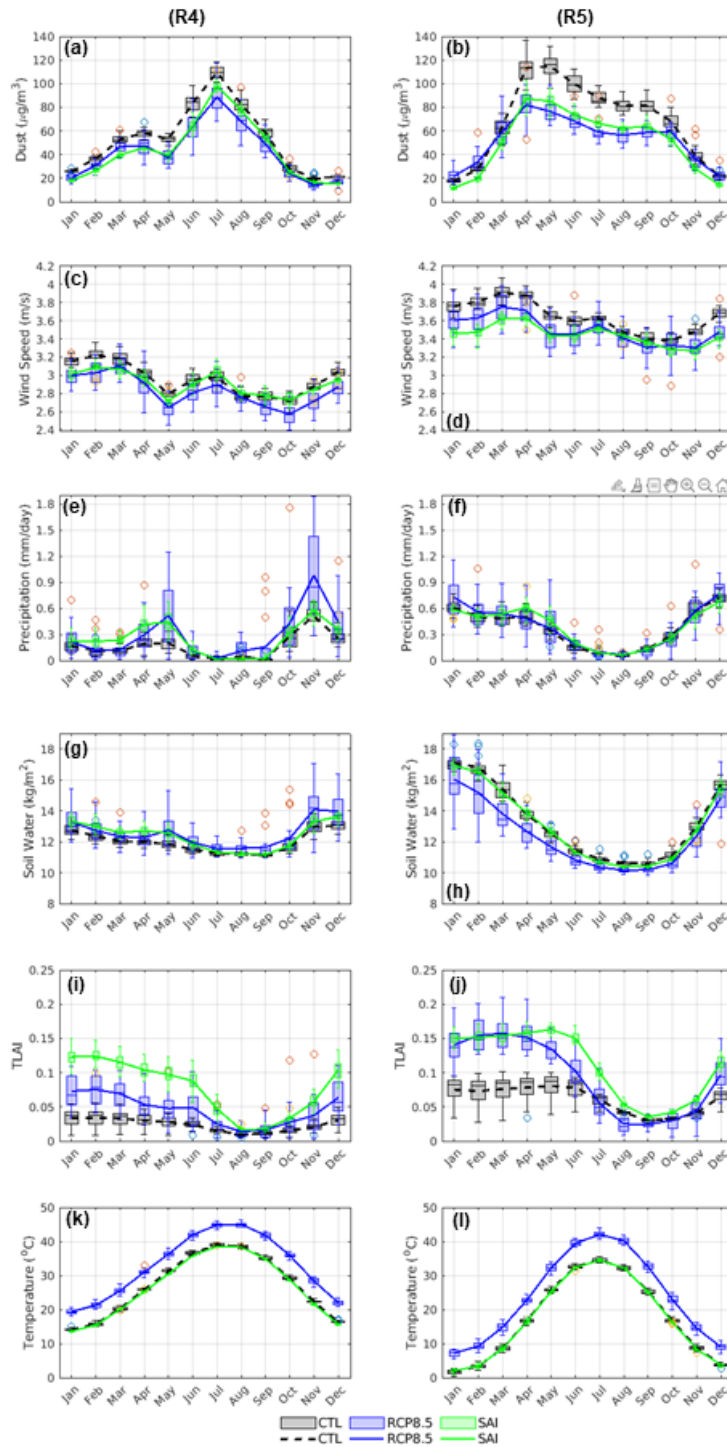
Figure 11: The multi monthly mean values of the considered parameters with percentile values as error bars for R4 dust hotspot (left column) and R5 dust hotspot (right column), for different scenarios. The box plots are depicted with the median (horizontal line), the 25–75 percentile (box), the 5–95 percentile (horizontal line), and outlier data (circle).